

Global 21 cm signal: a promising probe of primordial features

Suvedha Suresh Naik^{*},¹ Pravabati Chingangbam,^{1,2} Saurabh Singh,³ Andrei Mesinger,⁴ Kazuyuki Furuuchi⁵

¹Indian Institute of Astrophysics, Koramangala II Block, Bangalore 560 034, India

²Korea Institute for Advanced Study (KIAS), 85 Hoegiro, Dongdaemun-gu, Seoul, Republic of Korea-02455

³Raman Research Institute, Bangalore, India

⁴Scuola Normale Superiore, Piazza dei Cavalieri 7, I-56125 Pisa, Italy

⁵Manipal Centre for Natural Sciences, Manipal Academy of Higher Education, Manipal 576 104, Karnataka, India

E-mail: suvedha.naik@iiap.res.in, prava@iiap.res.in, saurabhs@rri.res.in,
andrei.mesinger@sns.it, kazuyuki.furuuchi@manipal.edu

Abstract. Inflationary models that involve bursts of particle production generate bump-like features in the primordial power spectrum of density perturbations. These features influence the evolution of density fluctuations, leaving their unique signatures in cosmological observations. A detailed investigation of such signatures would help constrain physical processes during inflation. With this motivation, the goal of this paper is two-fold. First, we conduct a detailed analysis of the effects of bump-like primordial features on the sky-averaged 21 cm signal. Using semi-numerical simulations, we demonstrate that the primordial features can significantly alter the ionization history and the global 21 cm profile, making them a promising probe of inflationary models. We found a special scale (namely, the turnover wavenumber, k^{turn}) at which the effect of primordial bump-like features on the global 21 cm profile vanishes. Also, we found that the behaviour of the primordial features on the global profile and ionization history are quite opposite for $k > k^{\text{turn}}$ and $k < k^{\text{turn}}$. We trace the root cause of these behaviours to the effects of primordial features on the halo mass function at high redshifts. Furthermore, we discuss the degeneracy between the astrophysical parameters and the primordial features in detail. Secondly, for a fixed set of astrophysical parameters, we derive upper limits on the amplitude of bump-like features in the range $10^{-1} < k [\text{Mpc}^{-1}] < 10^2$ using current limits on optical depth to reionization from CMB data by Planck.

^{*}Corresponding author.

Contents

1	Introduction	1
2	Primordial features due to particle productions during inflation	3
3	The global 21 cm profile	4
3.1	Semi-numerical Simulations of the 21 cm Signal	5
4	Global 21 cm signal as a probe of bump-like primordial features with fixed astrophysical parameters	7
4.1	Effects on $\langle x_{\text{HI}} \rangle$ and $\langle \delta T_b \rangle$	7
4.2	The Halo Mass Function in the presence of primordial features	9
5	Global 21 cm signal as a probe of bump-like primordial features with varying astrophysical parameters	12
5.1	Dependence of the turnover scale k^{turn} on the choice of astrophysical parameters	12
5.2	Comparison of the effects of bump models with EoR models	13
5.2.1	Ionization history	13
5.2.2	Global 21 cm profile	15
6	Constraining bump-like primordial features from Planck constraints on reionization history	17
7	Summary and Discussion	20
A	Effects of primordial features on the quantities contributing to the brightness temperature of the 21 cm signal	21
B	Relation between the peak of the primordial features and mass of the halos	23
C	Collapsed fraction of the halos	24

1 Introduction

Current observations of the Cosmic Microwave Background (CMB) and Large Scale Structures (LSS) are well explained by the theory of cosmic inflation [1–6]. According to the theory of inflation, primordial density perturbations originated as quantum fluctuations during inflation and evolved to form the structures in the universe. Therefore, cosmological observations are expected to carry imprints of the physical processes that occurred during inflation. Judicious extraction of this primordial information can then help to constrain models of inflation.

Despite the broad consistency between current observations and the Λ CDM model, characterized by a nearly scale-invariant primordial power spectrum, the data suggest possible deviations from scale-invariant behavior at specific spatial scales. Several classes of inflationary models predict scale-dependent features in the primordial power spectrum, commonly referred to as "primordial features" (see, e.g., [7, 8] and references therein). Testing these

models requires comparing their predictions with observations across different wavenumber ranges. Over the past two decades, several studies have sought to constrain primordial features within the wavenumber range $10^{-4} < k [\text{Mpc}^{-1}] < 0.2$, using CMB and LSS observations (see, e.g., [7, 9] for the latest results). The smaller scales corresponding to $1 < k [\text{Mpc}^{-1}] < 10$ are probed by the Lyman- α forest (see, e.g., [10] for constraints on dark matter models) and weak-lensing measurements [11, 12]. Scales beyond this region remain largely unconstrained at present.

In this work we focus on a class of theoretically well-motivated inflationary models involving bursts of particle production during inflation that predict bump-like features in the primordial power spectrum [13–19]. Such bursts of particle production may occur naturally in inflation models based on higher-dimensional gauge theories [17–19]. This strongly motivates searches for signatures of bump-like features in cosmological observations. The signatures of bump-like features have been investigated using CMB observations [20] and galaxy two-point correlation functions [21]. Currently available data provide upper limits on the amplitudes of these features in the range $10^{-4} < k [\text{Mpc}^{-1}] < 0.2$.

The 21 cm signal from the hyperfine transition of neutral hydrogen is expected to revolutionize our understanding of the physics of the early universe. The redshifted 21 cm signal will provide access to wavenumbers beyond those probed by current observations. Moreover, the tomographic nature of the signal will yield vast datasets to test theories governing inflation, cosmic dawn, and the Epoch of Reionization (EoR). Several ongoing and upcoming experiments aim to measure the power spectrum of the 21 cm signal at high redshifts, such as SKA [22], HERA [23], LEDA [24], LOFAR - 2.0 [25], MWA Phase II [26], NenuFAR [27], etc. Besides the power spectrum, experiments like EDGES [28], SARAS [29, 30], BIGHORNS [31], PRIZM [32], REACH [33], MIST [34], RHINO [35], etc., aim to measure the sky-averaged 21 cm signal from the cosmic dawn to the reionization epoch. In addition, there are several space-based proposals for studying the dark ages and cosmic dawn, such as ALO [36], ROLSES [37], LuSEE-night [38], PRATUSH [39], etc. The profile of the global 21 cm signal holds crucial information regarding the formation of the first stars and galaxies, heating of the IGM by X-ray photons, and the reionization of neutral hydrogen by UV photons and other physical processes [40]. Since the 21 cm signal from the high-redshift universe encodes the signatures of density fluctuations and astrophysical processes, it can serve as an important probe of inflationary models. Recently, ref. [41, 42] studied how the 21 cm signal can be used to probe the primordial power spectrum. Ref. [43] studied in detail the potential of the 21 cm signal to probe the matter power spectrum on small scales.

In a previous work by some of the authors [41], it was demonstrated that the 21 cm power spectrum, spanning multiple redshifts combined with expected noise from SKA-Low, has the potential to probe bump-like features within the range $0.1 \leq k [\text{Mpc}^{-1}] \leq 1.0$. In this work, we extend the previous analysis and focus on how the sky-averaged 21 cm signal can be used as a potential probe of bump-like features over a wider range of wavenumbers. We conduct a systematic analysis to examine the impact of bump-like primordial features on the global 21 cm signal using semi-numerical simulations. The presence of bump-like features in the primordial power spectrum enhances correlations in density fluctuations. Consequently, these features can significantly modify the reionization history and the global 21 cm profile, allowing us to investigate their signatures in the range $10^{-1} \lesssim k [\text{Mpc}^{-1}] \lesssim 10^2$. We find that the primary factor contributing to this modification is the change in the halo mass function, or the number density of halos, due to the addition of primordial features. Interestingly, we identify a specific scale where the effects of primordial features are nullified, with their impact

on the global 21 cm profile reversing above and below this scale. The distinct signatures of bump-like features on the evolution of the neutral fraction of hydrogen and the global 21 cm profile make them a promising probe of primordial features. Furthermore, the impact of primordial features on the reionization history enabled us to place upper limits on the amplitude of these features in the range $10^{-1} \lesssim k [\text{Mpc}^{-1}] \lesssim 10^2$, using *Planck*'s measurement of the optical depth to reionization.

The remainder of the paper is organised as follows: section 2 briefly discusses the parameterization of inflationary models that predict bump-like features. In section 3, we provide a brief overview of the global 21 cm profile and the details of our simulations. Section 4 presents our main results, showing the effects of primordial features on the ionization history and global 21 cm profiles, along with a detailed analysis to understand these effects. In section 5, we compare these effects with those arising from variations in the astrophysical parameters of the first stars and galaxies. Section 6 discusses the observational constraints on bump-like features obtained using the ionization history. Finally, in section 7, we summarise our results and comment on future directions.

2 Primordial features due to particle productions during inflation

The primordial scalar power spectrum assumed in the concordance Λ CDM model is given by

$$P_S = A_s \left(\frac{k}{k_*} \right)^{n_s - 1}, \quad (2.1)$$

where the pivot scale is typically chosen as $k_* = 0.05 \text{ Mpc}^{-1}$, and A_s and n_s parameterize the amplitude and spectral tilt of the power spectrum, respectively. From *Planck* data, we obtain $\ln(10^{10} A_s) = 3.044 \pm 0.014$ and $n_s = 0.9649 \pm 0.0042$ at 68% confidence level [7].

We study a class of inflation models [13–19] in which the inflaton field ϕ is coupled to a real scalar field χ through the interaction term

$$g^2(\phi - \phi_0)^2 \chi^2, \quad (2.2)$$

where g is the dimensionless coupling constant. When the inflaton field value crosses $\phi = \phi_0$, a burst of χ particle production occurs as they become instantaneously massless. When such an event occurs during the observable range of e -folds of inflation, it manifests in the primordial power spectrum as a bump-like feature.

We parameterize the primordial power spectrum with bump-like features by including the dominant and subdominant contributions to the power spectrum, calculated analytically with one-loop approximations [16]:

$$P_S = A_s \left(\frac{k}{k_*} \right)^{n_s - 1} + A_{\text{I}} \sum_i \left(\frac{f_1(x_i)}{f_1^{\text{max}}} \right) + A_{\text{II}} \sum_i \left(\frac{f_2(x_i)}{f_2^{\text{max}}} \right), \quad (2.3)$$

where A_{I} and A_{II} are amplitudes of dominant and subdominant contributions, respectively. The amplitudes depend on the coupling parameter as

$$A_{\text{I}} \simeq 6.6 \times 10^{-7} g^{7/2}, \quad (2.4)$$

$$A_{\text{II}} \simeq 1.1 \times 10^{-10} g^{5/2} \ln \left(\frac{g}{0.0003} \right)^2. \quad (2.5)$$

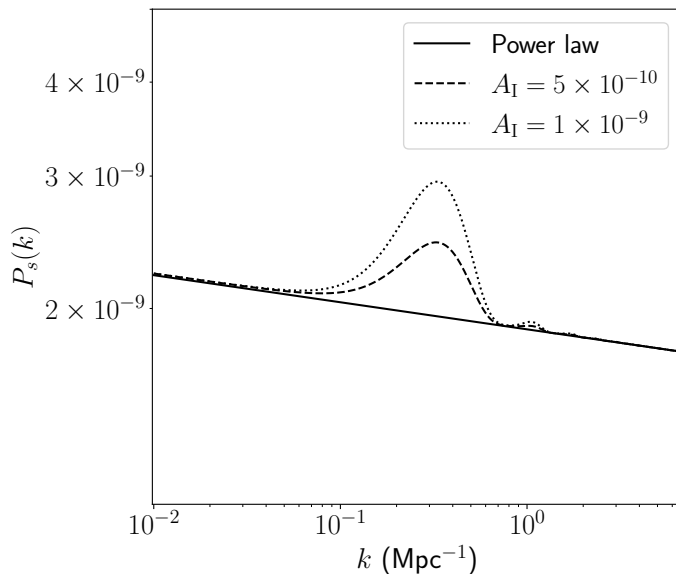


Figure 1: The primordial power spectrum with a bump-like feature at $k_{\text{peak}} = 0.3 \text{ Mpc}^{-1}$ is shown by dashed and dotted curves for $A_{\text{I}} = 1.0 \times 10^{-9}$ and 5.0×10^{-10} , respectively. The primordial power spectrum for the power law as in eq. (2.1) is plotted as a solid line.

The scale dependence of the contributions is given by the dimensionless functions

$$f_1(x_i) \equiv \frac{[\sin(x_i) - \text{SiIntegral}(x_i)]^2}{x_i^3}, \quad (2.6)$$

$$f_2(x_i) \equiv \frac{-2x_i \cos(2x_i) + (1 - x_i^2) \sin(2x_i)}{x_i^3}, \quad (2.7)$$

where $x_i \equiv \frac{k}{k_i}$. The parameter $k_i [\text{Mpc}^{-1}]$ is related to the position of the i^{th} feature on the primordial power spectrum, which peaks around $3.35 \times k_i$, and we define

$$k_{\text{peak},i} = 3.35 \times k_i. \quad (2.8)$$

For simplicity, in this paper, we focus on the case of a single episode of particle production during inflation, leading to a single bump-like feature on the primordial power spectrum with amplitude A_{I}^1 and peak location $k_{\text{peak}} [\text{Mpc}^{-1}]$. Figure 1 shows a comparison of such a power spectrum with the fiducial nearly scale-invariant form.

3 The global 21 cm profile

In this section, we provide a brief overview of the global 21 cm profile followed by the details of the simulations employed in this study. Theoretical models and numerical simulations based on radiative processes in the high-redshift universe have provided predictions for the expected

¹The subdominant amplitude A_{II} is not an independent parameter and can be written as $A_{\text{II}} \simeq (2.9 \times 10^{-6}) A_{\text{I}}^{5/7} [\ln A_{\text{I}}^{4/7} + 24]$.

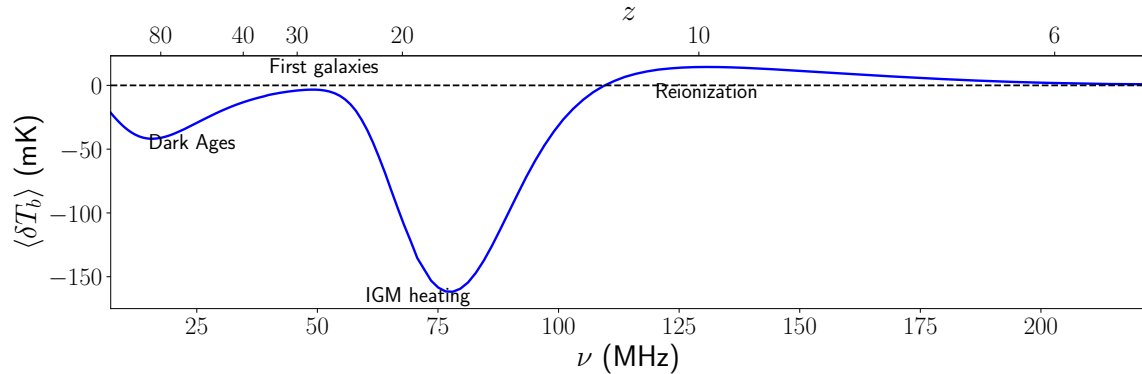


Figure 2: The time evolution of the sky-averaged 21 cm signal predicted from theoretical models and simulated with 21cmFAST [50].

evolution of the sky-averaged 21 cm signal, spanning from the dark ages to the completion of reionization (see, e.g., [44–47] for comprehensive reviews).

In the Rayleigh-Jeans approximation, the specific intensity of 21 cm radiation originating from neutral hydrogen (HI) can be expressed in terms of its brightness temperature (T_b). The differential brightness temperature δT_b , which captures the contrast between the spin temperature T_S and background radiation T_γ , is given by (e.g., [44, 48, 49]):

$$\delta T_b(z) \approx 27 x_{\text{HI}} (1 + \delta_{\text{nl}}) \left(\frac{H(z)}{dv_r/dr + H(z)} \right) \left(1 - \frac{T_\gamma}{T_S} \right) \left(\frac{1+z}{10} \frac{0.15}{\Omega_m h^2} \right)^{1/2} \left(\frac{\Omega_b h^2}{0.023} \right) \text{ mK}, \quad (3.1)$$

where δ_{nl} represents the fractional baryon density perturbation, x_{HI} denotes the neutral hydrogen fraction, $H(z)$ is the Hubble parameter, and dv_r/dr is the line-of-sight component of the proper velocity gradient. The spin temperature, T_S , describes the relative population of atoms in the two hyperfine levels. Thus, the observable quantity - the differential brightness temperature of the 21 cm signal - is shaped by the underlying density fluctuations, as well as the physical processes driving the formation of the earliest luminous sources and the reionization of the universe.

The simplest fundamental quantity used to characterize the 21 cm signal is the sky-averaged 21 cm brightness temperature, denoted by $\langle \delta T_b \rangle$, and its evolution across different redshifts, i.e., the global 21 cm profile. The evolution of $\langle \delta T_b \rangle$ obtained from a simulation of a representative theoretical model, is shown in figure 2, with some significant physical stages highlighted. The global profile includes absorption and emission features, whose amplitude and timing depend significantly on the underlying astrophysical processes [44, 48, 49]. The initial density fluctuations are influenced by cosmology through the primordial power spectrum, while the evolution of the quantities δ_{nl} , x_{HI} , and T_S is determined by astrophysical processes.

3.1 Semi-numerical Simulations of the 21 cm Signal

We utilize 21cmFASTv3² [50, 51], a semi-numerical simulation code, to model the cosmological 21 cm signal. 21cmFAST employs simplified physical modeling to efficiently generate realizations of the density, ionization, spin temperature fields, and velocity gradients, which are then combined to calculate the brightness temperature of the 21 cm signal using eq. (3.1).

²<https://github.com/21cmfast/21cmFAST>

We adopt the Friedmann-Lemaître-Robertson-Walker cosmological framework with flat spatial geometry. The concordance Λ CDM model is defined by several key parameters: the baryon density $\omega_b = \Omega_b h^2$, the cold dark matter density $\omega_{\text{cdm}} = \Omega_{\text{cdm}} h^2$, the present Hubble parameter H_0 , the optical depth to reionization τ_e , the amplitude of scalar perturbations A_s at the pivot scale $k_* = 0.05 \text{ Mpc}^{-1}$ (or alternatively σ_8 , the variance of density perturbations within a sphere of radius $8h^{-1} \text{ Mpc}$), and the spectral index n_s .

As mentioned previously, the brightness temperature of the 21 cm signal is affected by astrophysical processes, which are modeled through several parameters in 21cmFAST. Those discussed frequently in this paper are:

- M_{min} - the halo mass below which the abundance of active star-forming galaxies is exponentially suppressed. M_{min} (in solar mass units M_{\odot}) is often expressed in terms of the virial temperature T_{vir} (K) as [49]

$$M_{\text{min}} = 10^8 h^{-1} \left(\frac{\Omega_m}{\Omega_{m,z}} \frac{\Delta_{c,z}}{18\pi^2} \right)^{-1/2} \left(\frac{T_{\text{vir}}(\text{K})}{1.98 \times 10^4 \text{K}} \right)^{3/2} \left(\frac{1+z}{10} \right)^{-3/2} M_{\odot}, \quad (3.2)$$

where

$$\Omega_{m,z} = \Omega_m \left[\frac{(1+z)^3}{\Omega_m(1+z)^3 + \Omega_{\Lambda}} \right],$$

$$\Delta_{c,z} = 18\pi^2 - 39d_z^2 + 82d_z,$$

where $d_z = \Omega_{m,z} - 1$.

- ζ - the ionizing efficiency of high- z galaxies modelled as

$$\zeta = 30 \left(\frac{f_{\text{esc}}}{0.12} \right) \left(\frac{f_*}{0.05} \right) \left(\frac{N_{\gamma}}{4000} \right) \left(\frac{1.5}{1+n_{\text{rec}}} \right), \quad (3.3)$$

where f_{esc} is the fraction of ionizing photons that escape into the IGM, f_* is the fraction of galactic gas into stars, N_{γ} quantifies the ionizing photons per baryons and n_{rec} gives the typical number of recombination.

- $L_{X<2\text{keV}}/\text{SFR}$ - the normalization of the soft-band X-ray luminosity per unit star formation computed over the band 2 keV.

Other parameters that are used for modelling the reionization in 21cmFAST are: α_{esc} - the power-law index of f_{esc} , α_* - the power-law scaling of f_* with halo mass, t_* - the star formation time-scale taken as a fraction of the Hubble time, and E_0 - the lowest energy of the X-ray photon that can escape the galaxy.

Fiducial model: We define our base model, or the *fiducial model*, as follows: the concordance Λ CDM parameters are fixed using the best-fit values from the *Planck* 2018 results [7]³: $\Omega_b h^2 = 0.022$, $\Omega_{\text{cdm}} h^2 = 0.120$, $h = 0.6736$, $\tau_e = 0.058$, $\sigma_8 = 0.811$ and $n_s = 0.965$. We set the astrophysical parameters according to [52]: $M_{\text{min}} = 5 \times 10^8 M_{\odot}$ or $\log T_{\text{vir}} = 4.69897$, $\zeta = 30$ (i.e., $f_{\text{esc}} = 0.1$, $f_* = 0.05$, and $N_{\gamma} = 5000$), $\alpha_* = 0.5$, $\alpha_{\text{esc}} = -0.5$, $t_* = 0.5$, $E_0 = 0.5 \text{ keV}$, and $L_{X<2\text{keV}}/\text{SFR} = 10^{40.5} \text{ erg s}^{-1} M_{\odot}^{-1} \text{ yr}$. In 21cmFAST, the primordial power spectrum is calculated using the default power-law form [53, 54].

³The best-fit values obtained by combining data from temperature, polarization, and lensing.

In all our simulations, we select a simulation box length of 300 Mpc, beginning with a higher-resolution box containing 300 cells, which is then downsampled to a lower-resolution box with 100 cells. This configuration yields a resolution of 3 Mpc. The selected box length and cell size provide a compromise between the typical resolution from observations and feasible computational time. We simulate the brightness temperature across the redshift range $5 \lesssim z \lesssim 35$, incorporating calculations of the spin temperature.

4 Global 21 cm signal as a probe of bump-like primordial features with fixed astrophysical parameters

As described in section 2, we parameterize the bump-like primordial features by the amplitude of the bump, A_{I} , and the location of the peak of the bump denoted as k_{peak} . The theoretically estimated upper limit on the coupling parameter is given by $g^2 \lesssim 3$ [16], which imposes a constraint on A_{I} via equation (2.4), resulting in $A_{\text{I}} < 10^{-6}$. The parameter k_{peak} is not constrained by theoretical models. Since the bump-like primordial features are already constrained at the scales observed with the CMB in ref. [20], we explore scales beyond 0.1 Mpc^{-1} . Thus, our analysis encompasses models in the parameter ranges: $A_{\text{I}} \sim [10^{-10}, 10^{-7}]$ and $k_{\text{peak}} \geq 0.1 \text{ Mpc}^{-1}$. In this section, we keep the parameters of the astrophysical model fixed to the values of the “fiducial” model given in section 3.1 so as to cleanly investigate the effect of the primordial features. We revisit the effects of varying the astrophysical parameters in section 5.

4.1 Effects on $\langle x_{\text{HI}} \rangle$ and $\langle \delta T_{\text{b}} \rangle$

We begin by examining the effects of bump-like features on the averaged neutral hydrogen fraction $\langle x_{\text{HI}} \rangle$ and brightness temperature of the 21 cm signal $\langle \delta T_{\text{b}} \rangle$. In figure 3, we present the redshift evolution of $\langle x_{\text{HI}} \rangle$ and $\langle \delta T_{\text{b}} \rangle$, for various values of k_{peak} (indicated in each panel) and amplitudes A_{I} (represented by different line styles).

The impact of bump-like features on both $\langle x_{\text{HI}} \rangle$ and $\langle \delta T_{\text{b}} \rangle$ can be substantial. The ionization histories, depicted by the redshift evolution of $\langle x_{\text{HI}} \rangle$, show that k_{peak} affects the timing of the completion of reionization. As k_{peak} increases, its effect transitions from late reionization to early reionization, relative to the fiducial model. We observe that this turnover of effects of primordial features occurs around the scale $k^{\text{turn}} \sim 0.5 \text{ Mpc}^{-1}$ for the current choice of the fiducial model. We will refer to this scale as the “turnover scale” hereafter. We find a similar effect of k_{peak} on $\langle \delta T_{\text{b}} \rangle$ which also exhibits a transition around the same turnover scale. This special scale k^{turn} is crucial for our subsequent discussion as it marks the division of the effects of bump-like features into two distinct wavenumber regimes:

- $k_{\text{peak}} < k^{\text{turn}}$: As seen in the top two rows of figure 3, a smaller value of k_{peak} corresponds to a relatively delayed end of reionization compared to the fiducial model. Then for fixed k_{peak} , increasing A_{I} has the effect of increasing the delay of reionization, as seen in the plots of $\langle x_{\text{HI}} \rangle$. For $\langle \delta T_{\text{b}} \rangle$ we obtain a systematic shift of the profile towards lower redshifts. This shift is associated with a broadening of the width of the absorption trough and shallowing of the depth. Further, the rate of change with respect to A_{I} increases with increasing difference of k_{peak} from k^{turn} .
- $k_{\text{peak}} > k^{\text{turn}}$: In this regime, as shown by the last two rows of figure 3, we obtain trends in the behaviour of both $\langle x_{\text{HI}} \rangle$ and $\langle \delta T_{\text{b}} \rangle$ that are opposite to the above regime.

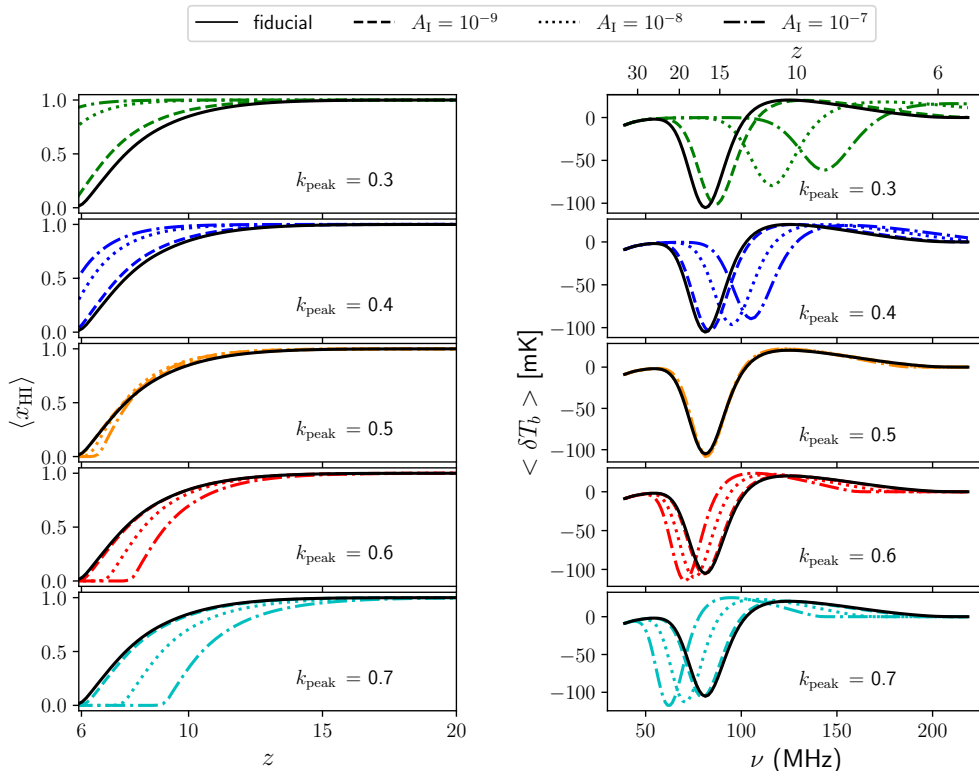


Figure 3: [Left] The ionization histories and [right] the global 21 cm profiles for single bump models at different values of k_{peak} . Each row corresponds to a specific k_{peak} value, with variations in the amplitude parameter A_{I} indicated by different line styles. The solid black curve represents the fiducial model without primordial features.

- $k_{\text{peak}} \sim k^{\text{turn}}$: For this special scale, the curves of both $\langle x_{\text{HI}} \rangle$ and $\langle \delta T_b \rangle$, corresponding to different values of A_{I} , are indistinguishable from the fiducial model (see middle panels of both columns of figure 3). This wavenumber thus represents a critical scale at which the bump-like features exert no significant influence on the profile of the global 21 cm signal.

Having discovered the existence of the interesting scale k^{turn} , we next investigate its physical origin. Since δT_b contains contributions from density fluctuations δ_{nl} , spin temperature T_S and neutral fraction of hydrogen x_{HI} , we examine the effect of the bump-like feature on these quantities separately. The details are provided in appendix A. All of these quantities depend on the collapsed fraction, $f_{\text{coll}}(z)$ - the fraction of gas inside collapsed objects at redshift z , which in turn is derived using the halo mass functions. Therefore, understanding the effect of primordial features on the halo mass function is key to understanding the physical origin of k^{turn} . This is what we address in the next subsection.

4.2 The Halo Mass Function in the presence of primordial features

The Halo Mass Function (HMF) denoted as $\frac{dn}{d\ln M}$ [Mpc^{-3}], represents the co-moving number density of halos in the mass range M to $(M + dM)$, and is given by [55]

$$\frac{dn}{d\ln M} = \frac{\rho_m}{M} \frac{-d(\ln \sigma)}{dM} \nu f(\nu), \quad (4.1)$$

where ρ_m represents the average matter density at $z = 0$ and $\nu \equiv \frac{\delta_c}{D(z)\sigma(M)}$, where δ_c is the critical overdensity, $D(z)$ is the growth factor. $\sigma(M)$ is the variance of the initial density fluctuation field, which is linearly extrapolated to the present epoch and smoothed with a filter $W(kR)$ of scale R . It can be expressed as

$$\sigma^2(R) = \frac{1}{2\pi^2} \int_0^\infty dk k^2 P_m(k) W^2(kR), \quad (4.2)$$

where $P_m(k)$ is the matter power spectrum. In 21cmFAST, a real space top-hat filter is used by default, whose Fourier transform is given by

$$W(kR) = 3 \left[\frac{\sin(kR) - (kR) \cos(kR)}{(kR)^3} \right], \quad (4.3)$$

where the radius of the top-hat filter, R , is given by

$$R(M) \equiv \left[\left(\frac{3}{4\pi} \right) \left(\frac{M}{\rho_m} \right) \right]^{1/3}. \quad (4.4)$$

In 21cmFAST, the Sheth-Tormen formula [56] for the HMF is used to calculate the number density of halos. In this formalism, the term $\nu f(\nu)$ in eq. (4.1) is given by

$$\nu f(\nu) = \sqrt{2\pi} A \left(1 + \frac{1}{\hat{\nu}^{2q}} \right) \hat{\nu} \exp \left(\frac{-\hat{\nu}^2}{2} \right), \quad (4.5)$$

where $\hat{\nu} = \sqrt{a}\nu$. The parameter values $a = 0.73$, $q = 0.175$ and $A = 0.353$ are used in the simulations, following [57]. The critical overdensity in the definition of ν above involves Sheth-Tormen correction following [56]. Note that the HMF given by eq. (4.1) varies with redshift with the redshift dependence entering via the terms that depend on $D(z)$ on the right hand side. Overall, there is an amplitude increase as the redshift decreases which is proportional to $D^{-2}(z)$, while the shape also gets scaled via the D factors that enter in eq. (4.5).

Eq. (4.1) tells us that the effect of the bump model on the HMF can be traced back to $\sigma^2(M)$. Before proceeding, we note that two halo-mass scales that are important for the discussion here. The first is M_{\min} , as given in eq. (3.2). Structure formation is driven by halos whose mass M_h is above M_{\min} . Of such halos, the lower mass ones in the vicinity of M_{\min} are much more numerous than the high mass ones (see the plot of HMF in panel (c) of figure 4). Hence, any physical process that impacts such lower mass halos more than high mass ones will leave a relatively stronger imprint on the HMF. Secondly, we can associate a halo mass scale, M_{peak}^R with a given value of k_{peak} by equating the right-hand side of eq. (4.4) to $2\pi/k_{\text{peak}}$. Thus, k_{peak} and M_{peak}^R are anti-correlated (see figure 14 in appendix B). We can anticipate that the effect of the primordial bump on physical observables will typically peak around this mass scale. The peak will be accompanied by a corresponding range of M_h over

which the effect will be felt⁴. The location of M_{peak} and the range of influence relative to M_{min} will determine the effect the primordial bump has on the HMF. We now quantify how the bump models affect the HMF, which in turn will explain the effect on $\langle x_{\text{HI}} \rangle$ and $\langle \delta T_b \rangle$ observed in the previous subsection.

In panel (a) of figure 4, we plot $\sigma^2(M)$ obtained from 21cmFAST for the fiducial and bump models extrapolated to $z = 0$. $M_{\text{min}} = 5 \times 10^8 M_{\odot}$ is shown by the black vertical dotted line. The black dot-dash line marks the mass value $M \simeq 2.8 \times 10^{14} M_{\odot}$, which corresponds to the scale of the power spectrum normalization, $8 h/\text{Mpc}$. The values of σ^2 for all models coincide at this mass value. Panel (b) shows the fractional difference $\delta\sigma^2(M)$ between the bump models and the fiducial one for some values of k_{peak} . Here, two points are worth mentioning. First of all, with increasing k_{peak} , the peak of the profiles, $M_{\text{peak}}^{\sigma^2}$, shifts toward the low-mass side, which can be understood by the relation between k_{peak} and M_{peak}^R , as discussed earlier (see appendix B for details). Secondly, there is an overall shift up of the entire profile on the vertical axis, which is primarily due to the normalization of the power spectrum at $8 h/\text{Mpc}$. Furthermore, $k_{\text{peak}} = 0.5 = k_{\text{turn}}$ roughly marks the value where the left tail of the profile transitions from negative to positive values of $\delta\sigma^2(M, z = 0)$ at $M_h = M_{\text{min}}$.

Next, we examine the effects of primordial bump-like features on the HMFs. Panel (c) of figure 4 shows the HMF curves for the fiducial and bump models for the same range of k_{peak} as the left column. M_{min} is again shown by the black vertical dotted lines. Panel (d) shows the fractional differences of the HMF between the bump and fiducial models for various values of k_{peak} , for $z = 15$ and 13 . With increasing k_{peak} , the peak of the profile, $M_{\text{peak}}^{\text{HMF}}$, shifts toward the low-mass scale, accompanied by a broadening of the profile. The peak locations $M_{\text{peak}}^{\text{HMF}}$ are roughly an order of magnitude higher than $M_{\text{peak}}^{\sigma^2}$ (refer to figure 14 in appendix B). This is because the HMF is related to the derivative of $\sigma(M)$. The broadening of the profiles with increasing k_{peak} is due to the factor $\nu f(\nu)$ in the expression for the HMF. Again, $k_{\text{peak}} = 0.5 = k_{\text{turn}}$ roughly marks the value where the left tail of the profile transitions from negative to positive values. We find a drop in the amplitude from $z = 15$ to 13 without changes in the peak locations. The implication of the above-observed behaviour of the HMFs is that, for $k_{\text{peak}} < k_{\text{turn}}$, there will be fewer halos having $M_h > M_{\text{min}}$ for the bump model relative to the fiducial power spectrum. This means that, at a given z , the bump model will be in a less advanced stage of reionization compared to the fiducial model. For $k_{\text{peak}} > k_{\text{turn}}$, the situation is reversed, and we should obtain a more advanced reionization for the bump model. This trend is exactly what we observe in figure 3. The effects of primordial features on the collapsed fraction of halos also show a similar trend and is discussed in appendix C.

To summarize, the effect of the primordial bump-like features on observable quantities such as ionization history and global 21 cm profile is driven by their effects on the HMF (primarily on the low-mass scales set by M_{min}), which further depends on $\sigma^2(M)$. Due to the power spectrum normalization at $8 h/\text{Mpc}$, the enhancement of power at different scales introduced by the primordial features significantly alters the number density of halos and, consequently, the structure formation. We find a particular scale where the effects of primordial features do not show up in the global 21 cm profile, i.e., the turnover scale, k^{turn} . The turnover scale is also crucial as the bump-like features with $k_{\text{peak}} > k^{\text{turn}}$ induce early reionization, and $k_{\text{peak}} < k^{\text{turn}}$ result in late reionization. Since the value of M_{min} is influenced by the underlying EoR model chosen through the virial temperature T_{vir} , it is expected that

⁴As the width of the bump-like features in k -space is directly proportional to its location k_{peak} , its influence on the HMF will be a range of mass scales.

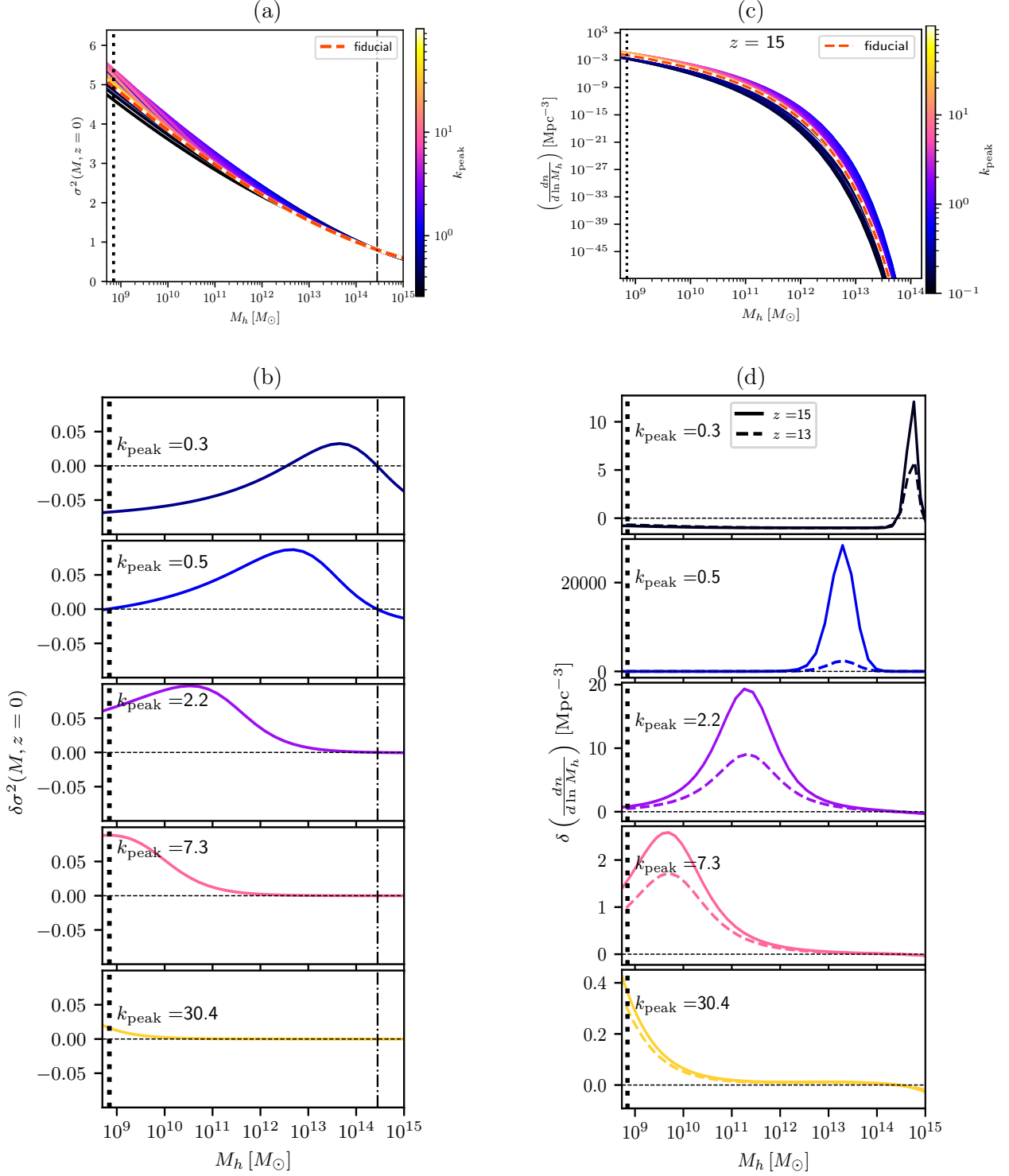


Figure 4: (a) $\sigma^2(M)$ extrapolated to $z = 0$ for the fiducial and bump models corresponding to our range of k_{peak} . The black dotted vertical line indicates $M_{\text{min}} = 5 \times 10^8 M_\odot$, while the dot-dashed lines indicate the halo mass value $2.8 \times 10^{14} M_\odot$ corresponding to σ_8 . (b) The fractional difference $\delta\sigma^2(M)$ between bump and fiducial models. (c) The HMFs for the fiducial and bump models are shown for $z \sim 15$. The bump-like features have amplitude $A_{\text{I}} = 10^{-9}$. The fiducial model is shown in orange color. The black dotted vertical line indicates M_{min} . (d) The fractional differences of the HMF curves for the bump models in panel (b) relative to the fiducial model are shown for two redshifts, $z = 15$ and 13 . The turnover scale in this case is $k_{\text{peak}} = 0.5 \text{ Mpc}^{-1}$.

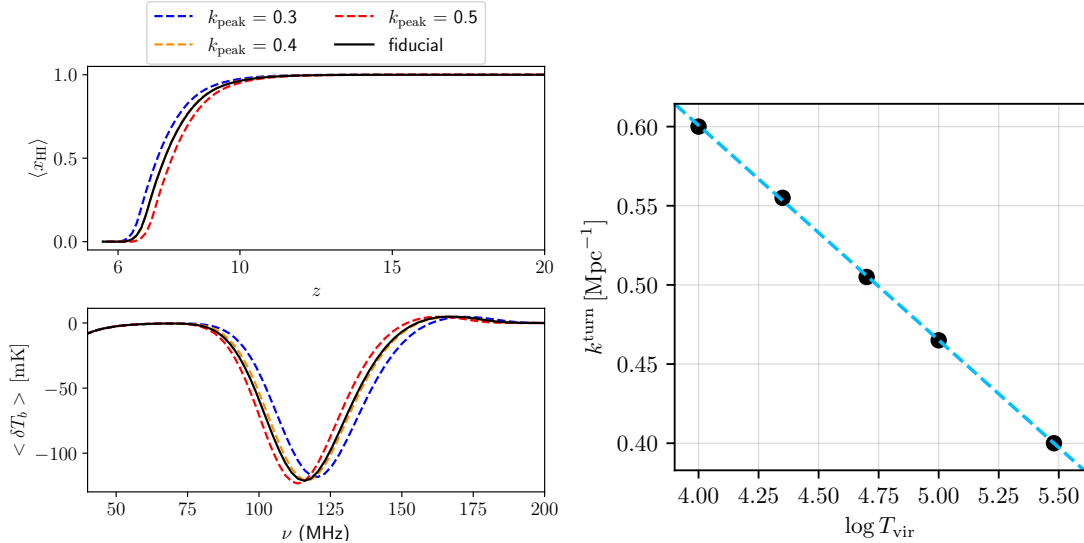


Figure 5: [Left] The ionization history and the global 21 cm profile for the bump models using the “bright” galaxies model as the fiducial. The amplitude of the features is fixed at $A_{\text{I}} = 10^{-9}$. [Right] Simulated values of k^{turn} for different T_{vir} values. L_X is fixed to 40.5 for this plot. The cyan dashed line represents a linear fit.

the value of k^{turn} may depend on T_{vir} , which we explore in the next section.

5 Global 21 cm signal as a probe of bump-like primordial features with varying astrophysical parameters

Having understood the effect of bump-like primordial features on the global 21 cm signal and the existence and physical origin of k^{turn} for fixed astrophysical parameters, we now turn our attention to investigating the effects when the astrophysical parameters are also varied. This exercise will reveal how k^{turn} will depend on the EoR parameters and any degeneracies and distinguishability of the effects of primordial features from the effects of different astrophysical parameters. We focus on three astrophysical parameters that crucially impact the ionization history and global 21 cm profile: the ionizing efficiency ζ , the virial temperature of the halos T_{vir} , and the soft-band X-ray luminosity per unit SFR L_X .

5.1 Dependence of the turnover scale k^{turn} on the choice of astrophysical parameters

For varying the EoR parameters, we follow the convention of “faint” and “bright” galaxies models, as given in [58]. In the “faint” galaxies model, the EoR parameter values are roughly $\zeta \sim 30$ and $T_{\text{vir}} \sim 5 \times 10^4$ K. The fiducial EoR model used in the previous section falls in this category. In contrast, in the “bright” galaxies model, structure formation is primarily driven by rare and relatively massive galaxies with the EoR parameter values $\zeta \sim 200$, $T_{\text{vir}} \sim 3 \times 10^5$ K. In the latter case, we have $M_{\text{min}} \approx 8 \times 10^9 M_{\odot}$ (roughly an order of magnitude higher than the faint galaxies model). Consequently, for such models, the influence on structure formation can be deciphered from the behaviour of the HMF at mass scales $M_h \gtrsim 8 \times 10^9 M_{\odot}$.

Since k_{peak} and M_h are inversely related, an increase in M_{min} is expected to cause a decrease in k^{turn} . To verify this, we calculate the ionization history and global 21 cm profile

for different values of T_{vir} . Note that since T_{vir} defines the mass range of galaxies involved in structure formation, in each case, the ionizing efficiency parameter ζ is appropriately adjusted to ensure that the optical depth to reionization, τ_e , is within the 95% limits measured by CMB observations from *Planck*. We fix L_X to be 40.5. The turnover scale k^{turn} is the value of k_{peak} for which the redshift of the minimum in the absorption trough of its global profile matches that of the fiducial model. The results are plotted in figure 5. On the left column, we plot $\langle x_{\text{HI}} \rangle$ (top) and $\langle \delta T_b \rangle$ (bottom) for the bright galaxies model with parameter values $\zeta = 200$ and $T_{\text{vir}} = 3 \times 10^5 \text{ K}$ for different values of k_{peak} . We observe in this case that the turnover scale is now 0.4 Mpc^{-1} , which, as expected, is lower than the value for the faint galaxies model.

The right column of figure 5 shows k^{turn} as a function of T_{vir} . The black dots are the actual calculations of k^{turn} from the simulations. From left to right, ζ is increasing from 10 to 200. The blue dashed line represents a straight-line fit⁵ given by the form $k^{\text{turn}} = \alpha + \beta(\log T_{\text{vir}})$.

We repeated the calculations for various values of L_X and found that its impact on k^{turn} is negligible. This is because k^{turn} is affected only when changes in astrophysical parameters cause a shift in the global profile compared to the fiducial case. While L_X influences heating and alters the depth of the absorption trough, T_{vir} causes a shift in the global profile. Thus, we conclude that for a given EoR model, there exists a specific scale k^{turn} , governed by T_{vir} , at which the bump-like features show negligible effects on the global 21 cm profile.

5.2 Comparison of the effects of bump models with EoR models

In this section, we explore how changes in EoR models, characterized by ζ , T_{vir} and L_X , affect the ionization history and the global 21 cm profile. The purpose is to compare such effects with the influence of bump-like features. We choose the parameter ranges for the EoR models as $\zeta \sim [10, 50]$, $\log T_{\text{vir}} \sim [4.4, 5.4]$, and $\log L_X \sim [38, 42]$. These ranges ensure that the predicted ionization history and 21 cm signal are consistent with theoretical expectations and observational constraints [58].

Figure 6 shows the effect of varying each EoR parameter, keeping the other two fixed at their fiducial values, on the reionization history (top panel) and the global 21 cm profile (bottom panel). Below, we further quantify the dependence of these observables on the EoR parameters.

5.2.1 Ionization history

We begin by quantifying the ionization history by plotting the redshift corresponding to 50% ionization, $z_{0.5}$ (i.e., $\langle x_{\text{HI}} \rangle = 0.5$) against different parameters, as shown in the top and bottom left panels of figure 7. Increasing ζ results in earlier reionization, leading to a higher $z_{0.5}$. In contrast, increasing T_{vir} results in a lower $z_{0.5}$. Since higher T_{vir} corresponds to larger M_{min} (eq. (3.2)), structure formation is driven by relatively massive galaxies with lower number density, delaying the end of reionization. We also find that L_X has little influence on the reionization history. For comparison, the effect of k_{peak} for bump-like features is shown in the bottom right panel for two values of A_I . We observe a trend distinct from the trend seen for the EoR parameters. With an increase in k_{peak} , $z_{0.5}$ increases and reaches the value of the fiducial model at $k \sim k^{\text{turn}}$. Beyond that, $z_{0.5}$ further increases till it reaches a maximum

⁵The best-fit parameters are $\alpha = 1.144$ and $\beta = -0.136$. α and β are likely to be physical quantities, and we will explore their meaning and the linear relation in the future.

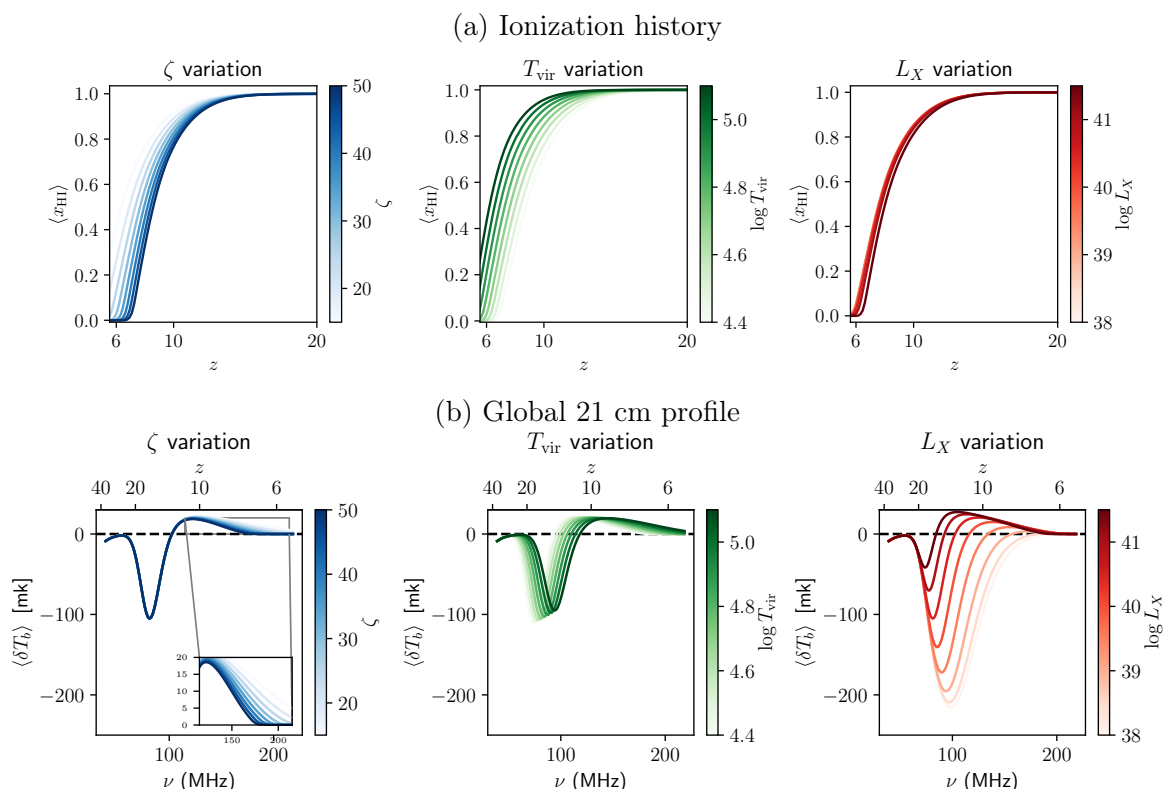


Figure 6: [Top] Ionization history and [bottom] global 21 cm profiles for the EoR models, illustrating the effects of varying ζ (left), T_{vir} (middle), and L_X (right). Increasing shade represents an increase in the magnitude of the parameter.

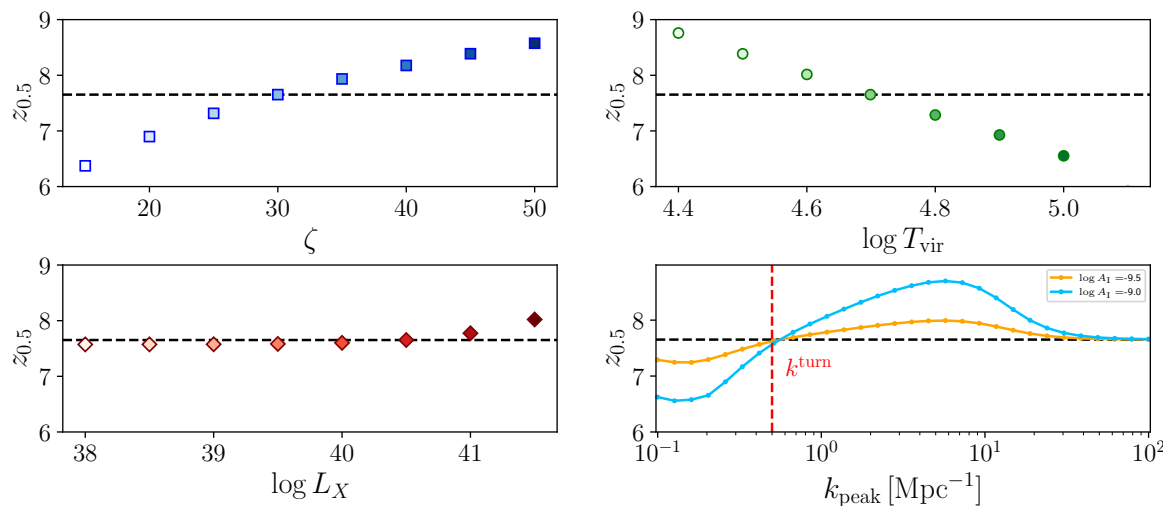


Figure 7: The redshifts corresponding to 50% reionization, $z_{0.5}$, plotted against the parameters of EoR and bump models. The horizontal dashed line represents $z_{0.5}$ for the fiducial model.

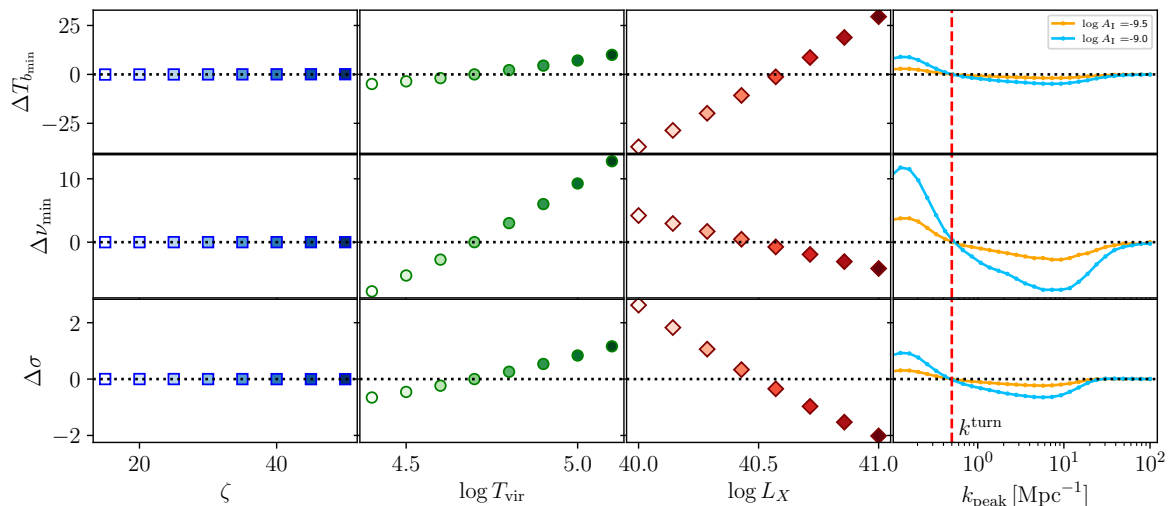


Figure 8: The relative shift in the parameters - depth of the absorption profile, $\Delta T_{b_{\min}}$ (top), frequency of the absorption trough, $\Delta \nu_{\min}$ (middle), and width of the profile, $\Delta \sigma$ (bottom), relative to the fiducial model, obtained by fitting a Gaussian profile.

when the mass scale corresponding to k_{peak} , i.e., M_{peak} , coincides with M_{min} and results in a maximum number density of low-mass halos in the HMF (refer to figure 4 (d)). As k_{peak} increases beyond this scale, only the tail of the bump affects the HMF, and consequently, $z_{0.5}$ decreases. Increasing the amplitude of the bump feature enhances the effect of k_{peak} . Visually, we notice that for low values of k_{peak} , the parameter ζ shows correlation, and T_{vir} shows anti-correlation with k_{peak} .

5.2.2 Global 21 cm profile

We parameterize the global 21 cm profile in two ways:

- Fitting the absorption trough of the signal to a Gaussian profile, characterized by amplitude $T_{b_{\min}}$, mean frequency ν_{\min} , and standard deviation σ .
- Identifying the average brightness temperatures $\langle \delta T_b \rangle$ and corresponding frequencies ν (or redshifts) at three key extrema points following [59].

The findings are discussed below.

(a) Fitting a Gaussian profile: We fit the absorption trough of the global profile to a Gaussian function and obtain $T_{b_{\min}}$, ν_{\min} and σ . The shift in these quantities for the models with varying EoR parameters or bump parameters relative to the fiducial model, i.e., $\Delta X = X^{\text{EoR/bump}} - X^{\text{fid}}$, where X is $T_{b_{\min}}$, ν_{\min} and σ , are plotted in the three rows of figure 8, respectively.

As seen in the bottom panels of figure 6, ζ primarily affects the EoR at $z < 15$, having minimal influence on the parameters defining the absorption trough. Increasing T_{vir} results in a profile shift toward higher frequencies (lower z), causing the absorption trough to become wider and shorter. The parameter L_X significantly alters the depth and width of the global 21 cm profile. As X-ray luminosity heats up the IGM, a higher value of L_X rapidly raises the kinetic temperature, which is coupled to the spin temperature T_S , above the background

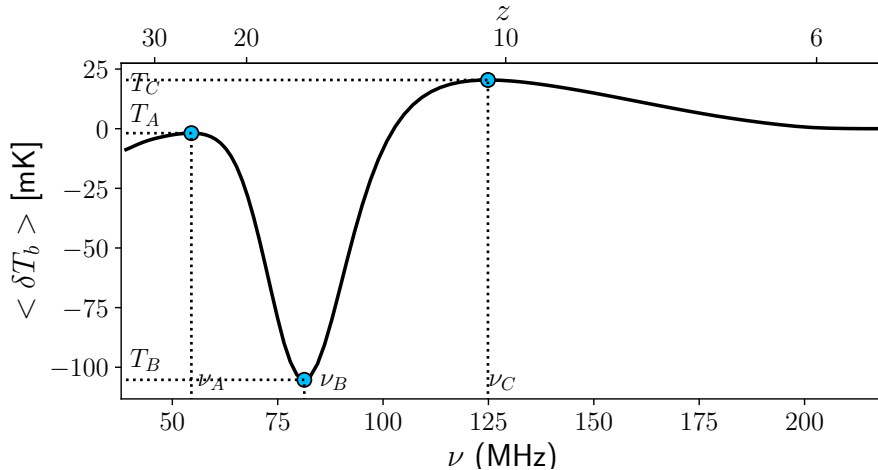


Figure 9: The points of extrema used for quantifying the global 21 cm signal in figure 10.

temperature T_γ , leading to an earlier emission signal. Thus, an increase in L_X contributes to the narrowing of the width and reduces the depth of the profile. These effects of ζ , T_{vir} and L_X are quantified and illustrated in the first three columns of figure 8 (left to right).

For comparison with the above, the effects of bump-like features are shown in the last column of figure 8 for the same two values of A_I as in figure 7. As previously noted, if $k_{\text{peak}} < k^{\text{turn}}$, the number density of halos is lower than that of the fiducial model, leading to delays in heating and reionization as described in section 4.2. Consequently, the global 21 cm profile shifts toward the high-frequency or low- z end. In contrast, if $k_{\text{peak}} > k^{\text{turn}}$, the number density of halos exceeds that of the fiducial model, resulting in a shift of profile toward the low-frequency. These effects become more pronounced with an increase in the amplitude of the primordial features.

As stated earlier, the above exercise aims to determine whether the primordial bump-like features can be distinguished from EoR parameters. First, we note that the correlation of ζ with k_{peak} noticed in the ionization history in figure 7 does not show up in the global profile. This indicates that the effects of primordial features can potentially be distinguished from the effects of ζ . Secondly, from a comparison between columns 3 and 4 of figure 8, we find that the effect of L_X can be clearly distinguished from k_{peak} . Finally, the anti-correlation of T_{vir} with k_{peak} noticed in figure 7 for the low k_{peak} values remains in figure 8. This means that changes to the global profile, such as increasing the depth of the absorption trough, shifting ν_{min} to higher frequency and broadening the profile, all of these can be achieved either by increasing T_{vir} or by introducing a primordial bump-like feature with a smaller k_{peak} .

(b) Points of extrema: We now quantify the global 21 cm profile by noting the average brightness temperatures and frequencies corresponding to the points of two maxima and one minimum following [59]. We refer to these points as T_A at $\nu = \nu_A$, T_B at $\nu = \nu_B$, and T_C at $\nu = \nu_C$, as shown in figure 9.

The top panel of figure 10 shows temperatures and frequencies related to points A, B, and C for the EoR models, while the bottom panel shows the same for bump models. The effect of ζ is significant only at point ‘C’, corresponding to the maximum of the profile in the low-redshift regime. The EoR models with varying L_X are placed along the diagonal of the plots for ‘B’ and ‘C’, showing no scatter in the plot of ‘A’. However, T_{vir} shows distinct

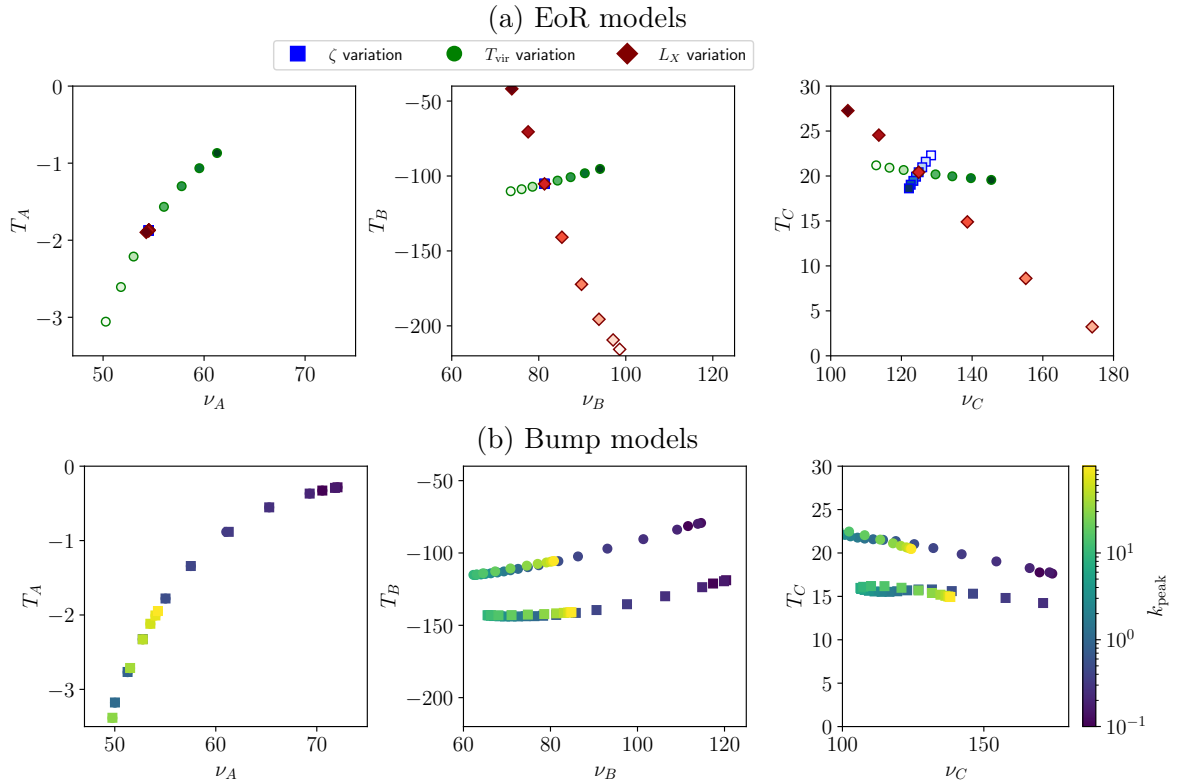


Figure 10: The average brightness temperature and frequency corresponding to points A, B and C in figure 9 are plotted in the left, middle and right panels, respectively. Plots in (a) show the variation of astrophysical parameters ζ , $\log T_{\text{vir}}$, $\log L_X$ and plots in (b) show the variation in k_{peak} with $A_{\text{I}} = 10^{-9}$. Increasing shade represents increase in magnitude of the parameter. The bump models are plotted for two sets of fiducial values: $L_X = 40.5$ is denoted by circles and $L_X = 40.0$ is denoted by squares.

trends in all three plots. On the bottom panel, the effect of variation of k_{peak} is shown for two different underlying EoR models: $L_X = 40.5$ is denoted by circles and $L_X = 40.0$ is denoted by squares. The points corresponding to the bump-like features with $k_{\text{peak}} > k^{\text{turn}}$ reflect as overlapping points in all the three plots of A, B and C, indicating degeneracy among the bump models on these scales.

Once again, in all of these plots, the bump models show a trend similar to that of T_{vir} , while the effects of ζ and L_X are clearly distinguishable. The degeneracy of the bump model with the virial temperature was expected as T_{vir} directly influences the effects of bump-like features on the global 21 cm profile through the mass threshold M_{min} . Therefore, higher-order statistics, such as the power spectrum may help break the degeneracy, which will be discussed in an upcoming work.

6 Constraining bump-like primordial features from Planck constraints on reionization history

In the previous sections, we emphasized that primordial bump-like features in the range $10^{-1} < k_{\text{peak}} [\text{Mpc}^{-1}] < 10^2$ can significantly affect the ionization history and the global 21

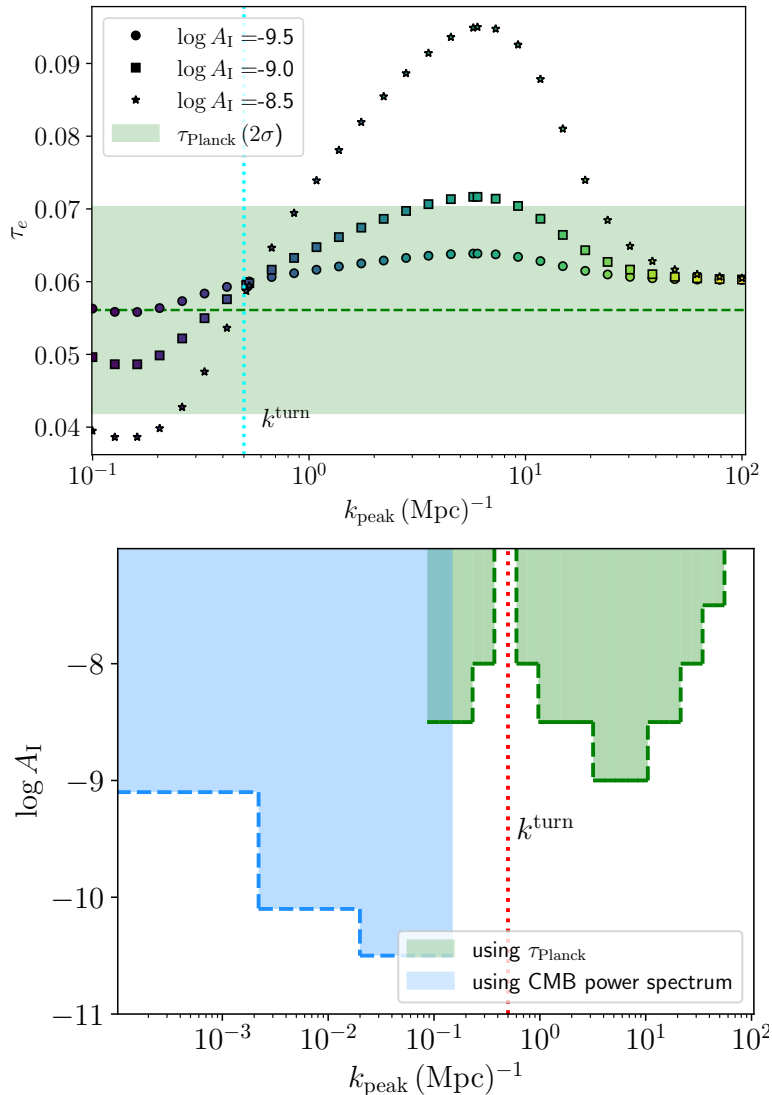


Figure 11: [Top] The optical depth to reionization τ_e predicted for bump-like models. The constraint on τ_e from Planck is shown by the dashed line, with the 95% confidence interval indicated by the shaded region. [Bottom] The upper limits on A_I in the range $10^{-4} < k \text{ [Mpc}^{-1}] < 0.15$ obtained from CMB data analysis in ref. [20] are shown by the blue shaded region. The new constraints on A_I in the range $10^{-1} < k \text{ [Mpc}^{-1}] < 10^2$ by comparing the τ_e values in this work are shown by the green shaded region.

cm profile. In this section, we explore constraints on the parameters A_I and k_b by comparing the simulations with the currently available observations on the reionization history. All the astrophysical parameters are fixed to their fiducial values in this analysis.

The CMB observations by *Planck* [60, 61] have imposed limits on the ionization of the high-redshift intergalactic medium (IGM) through the parameter - Thomson scattering optical depth, τ_e . As ionization progresses following the formation of the first stars and galaxies, CMB photons are scattered by free electrons in the IGM. Consequently, the observed CMB is influenced by the total column density of these free electrons along the line of sight. The

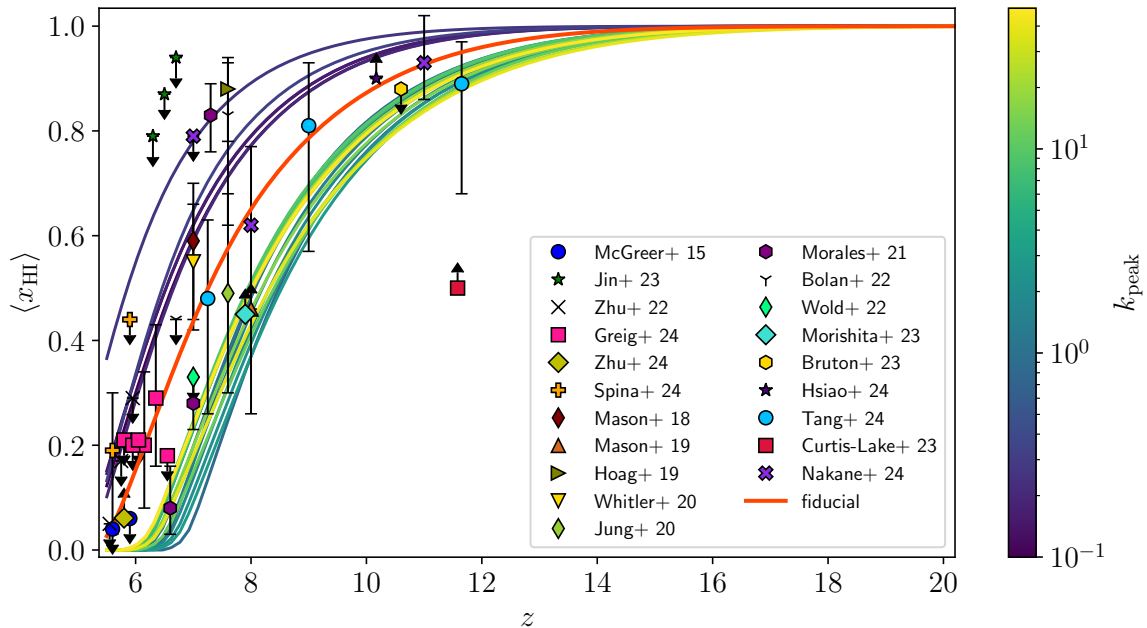


Figure 12: The solid curves show the reionization history for bump models with different k_{peak} (as indicated by the color bar) and upper limits on A_{I} , based on constraints using τ_e . The markers with error bars denote the 95% limits on the neutral fraction of hydrogen (with arrows representing upper/lower limits) from high- z quasars and Ly- α observations compiled from the literature [62–81].

reionization optical depth τ_e is constrained as one of the six parameters of the Λ CDM model. CMB observations by Planck indicate $\tau_{\text{Planck}} = 0.058 \pm 0.012$ (95% CL) [61]. We compute the values of τ_e for bump-like models using 21cmFAST and compare with τ_{Planck} to derive constraints on the parameters A_{I} and k_b .

Our results are shown on the top panel of Figure 11 with *Planck* constraints on τ_e shown by the shaded region. Different markers indicate the amplitude of the features A_{I} at a given k_{peak} . Within the 95% confidence interval, several bump-like models predict τ_e values inconsistent with the data, allowing us to exclude these models. On the bottom panel, upper limits on A_{I} are presented for each k_{peak} obtained from this analysis in the range of $k \sim [10^{-1}, 10^2]$. We also show our constraints from a detailed analysis using the CMB angular power spectrum (temperature and polarization data) [20] in the range $k \sim [10^{-4}, 0.15]$. Due to the distinct behaviour of bump-like features above and below k^{turn} , the constraints become weaker as k_{peak} approaches k^{turn} and become unconstrained at $k \sim k^{\text{turn}}$. The upper limit on A_{I} is the tightest when the features contribute maximally to the HMF, i.e., around $k \sim 7 \text{ Mpc}^{-1}$, and the amplitudes remain largely unconstrained at $k \gtrsim 70 \text{ Mpc}^{-1}$. We note that the observational constraints on A_{I} and k_{peak} depend on the underlying EoR model as k^{turn} depends on the virial temperature.

In addition to *Planck*, recent studies of high-redshift quasars and Ly- α observations have established constraints on the neutral hydrogen fraction across various redshifts. Figure 12 shows a compilation of observational constraints on the neutral fraction of hydrogen from high- z quasars and Ly- α observations [62–81]. We also plot the ionization history of bump models with the maximum allowed amplitude A_{I} inferred from τ_{Planck} . The predicted ionization

histories for the bump models almost lie within the observational uncertainties, providing no significantly tighter constraints.

7 Summary and Discussion

In this work, we analyzed the effects of features in the primordial power spectrum expected from particle production during inflation on the global 21 cm profile and the ionization history. The bump-like primordial features are parameterized by their amplitude A_{I} and the scale corresponding to the peak of the feature k_{peak} . Using the semi-numerical simulation code 21cmFAST [50, 51], we modify the power spectrum and simulate the ionization history and the global 21 cm profile for various values of A_{I} and k_{peak} .

The first part of our study is a detailed investigation of the impact of primordial bump-like features on the reionization history and the sky-averaged 21 cm signal. When the background EoR model is fixed, we found that introducing primordial bump-like features can significantly alter the ionization history of the universe and the global 21 cm profile (as shown in figure 3). The extent of deviation from the fiducial model is very sensitive to the scale at which the primordial feature peaks. An important finding is that, for a given EoR model, there exists a special turnover scale k^{turn} , which depends on the virial temperature T_{vir} (refer to figure 5) and controls the behaviour of primordial features on the 21 cm signal as follows:

- If k_{peak} is less than the scale k^{turn} , reionization ends later than the fiducial model. Also, the global 21 cm profile was found to shift toward low-redshift. An increase in the amplitude of the primordial feature enhances this effect.
- If k_{peak} is greater than k^{turn} , reionization ends earlier than the fiducial model and the global profile of 21 cm shifts toward the high-redshift side.
- When the primordial features peak around k^{turn} , the reionization history and the global 21 cm profile were almost unchanged compared to the fiducial model.

We found that the above-mentioned effects can be traced back to how the bump-like features influence structure formation at different redshifts. In section 4.2, we provide a detailed investigation of the effects of primordial features on the Halo Mass Function (HMF). Introducing bump-like features in the primordial power spectrum affects the variance of the smoothed density fluctuations, thereby impacting the HMF. In particular, the contribution of primordial features to the HMF in the low-mass regime ($M_h > M_{\text{min}}$) is important to understand the effects on structure formation. Our results show that if the primordial features have $k_{\text{peak}} < k^{\text{turn}}$, the tail of the feature affects the HMF in the low-mass regime such that the number density of halos is less than that of the fiducial model, leading to delayed reionization and a shift in the global 21 cm profile toward lower redshifts. Conversely, if $k_{\text{peak}} > k^{\text{turn}}$, the peak of the feature affects the low-mass range, increasing the number density of halos compared to the fiducial model. As a result, a larger number of low-mass galaxies participate in structure formation, causing reionization to complete earlier. At $k_{\text{peak}} \simeq k^{\text{turn}}$, the tail of the bump coincides with the fiducial model in the low-mass range of HMF, causing negligible effects on the global 21 cm signal.

The second part of our investigation compares the effects of primordial features with the effects of three astrophysical parameters: ionizing efficiency ζ , virial temperature T_{vir} , and X-ray luminosity L_X . Our main finding is that primordial bump-like features exhibit

degeneracy between T_{vir} and k_{peak} , with these two parameters being anti-correlated. On the other hand, ζ and L_X show distinguishable effects from the primordial features.

Lastly, by comparing the expected optical depth to reionization τ_e with the observed value from *Planck*, we derived upper limits on the amplitude of the features in the k range $[0.1, 100] \text{ Mpc}^{-1}$, assuming a fiducial EoR model. Our results in figure 11 indicate that the scale k^{turn} remains unconstrained, while the tightest upper limit is obtained for the scales where the features have the highest impact on the HMF in the low-mass range, i.e., for $k_{\text{peak}} \sim 7 \text{ Mpc}^{-1}$. Additionally, values of $k_{\text{peak}} > 70 \text{ Mpc}^{-1}$ are unconstrained as the effects of primordial features diminish in the HMF.

Future direction: We note that the effects of primordial bump-like features on the 21 cm signal are very sensitive to the scale at which they peak. The effect of k_{peak} on the ionization history and the global 21 cm profile can be mimicked up to a certain extent by tuning the parameter T_{vir} . This degeneracy and the fact that primordial bump models are unconstrained if $k_{\text{peak}} = k^{\text{turn}}$ are limitations when we try to constrain such models using the global 21 cm profile alone. Therefore, combining other observables, such as 21 cm power spectra, higher-order statistics, and morphological statistics, will be necessary to break this degeneracy. A detailed analysis of the effects of bump-like features on these observables will be presented in an upcoming work.

Besides the bump-like primordial features discussed in this work, other types of features, such as oscillatory, sharp rises, or dips in the primordial power spectrum, may leave unique signatures on the 21 cm signal. Since the variance of the density fluctuations involves the convolution of the power spectrum with a window function, the shape of the feature and the range of mass scales they affect will be important for estimating their HMF. Such a detailed study is worth investigating to check if future observations can distinguish the signatures of different inflationary models. This will be carried out as part of future work.

Acknowledgements

The computational work in this paper was carried out using the NOVA cluster at IIA, Bangalore. SSN is supported by the National Post Doctoral Fellowship by the Science and Engineering Research Board, Anusandhan National Research Foundation, Government of India, under the project file number PDF/2023/001469. KF acknowledges Manipal Centre for Natural Sciences, Centre of Excellence, Manipal Academy of Higher Education (MAHE) for facilities and support.

A Effects of primordial features on the quantities contributing to the brightness temperature of the 21 cm signal

In this section, we discuss the contributions of primordial features to density fluctuations δ_{nl} , spin temperature T_S and the neutral fraction of hydrogen x_{HI} , individually. The differential brightness temperature of the 21 cm signal is given by

$$\delta T_b \approx 27 x_{\text{HI}} (1 + \delta_{\text{nl}}) \left(\frac{H}{dv_r/dr + H} \right) \left(1 - \frac{T_\gamma}{T_S} \right) \left(\frac{1+z}{10} \frac{0.15}{\Omega_M h^2} \right)^{1/2} \left(\frac{\Omega_b h^2}{0.023} \right) \text{ mK}. \quad (\text{A.1})$$

To understand how the quantities δ_{nl} , T_S and x_{HI} affect the sky-averaged 21 cm signal, we

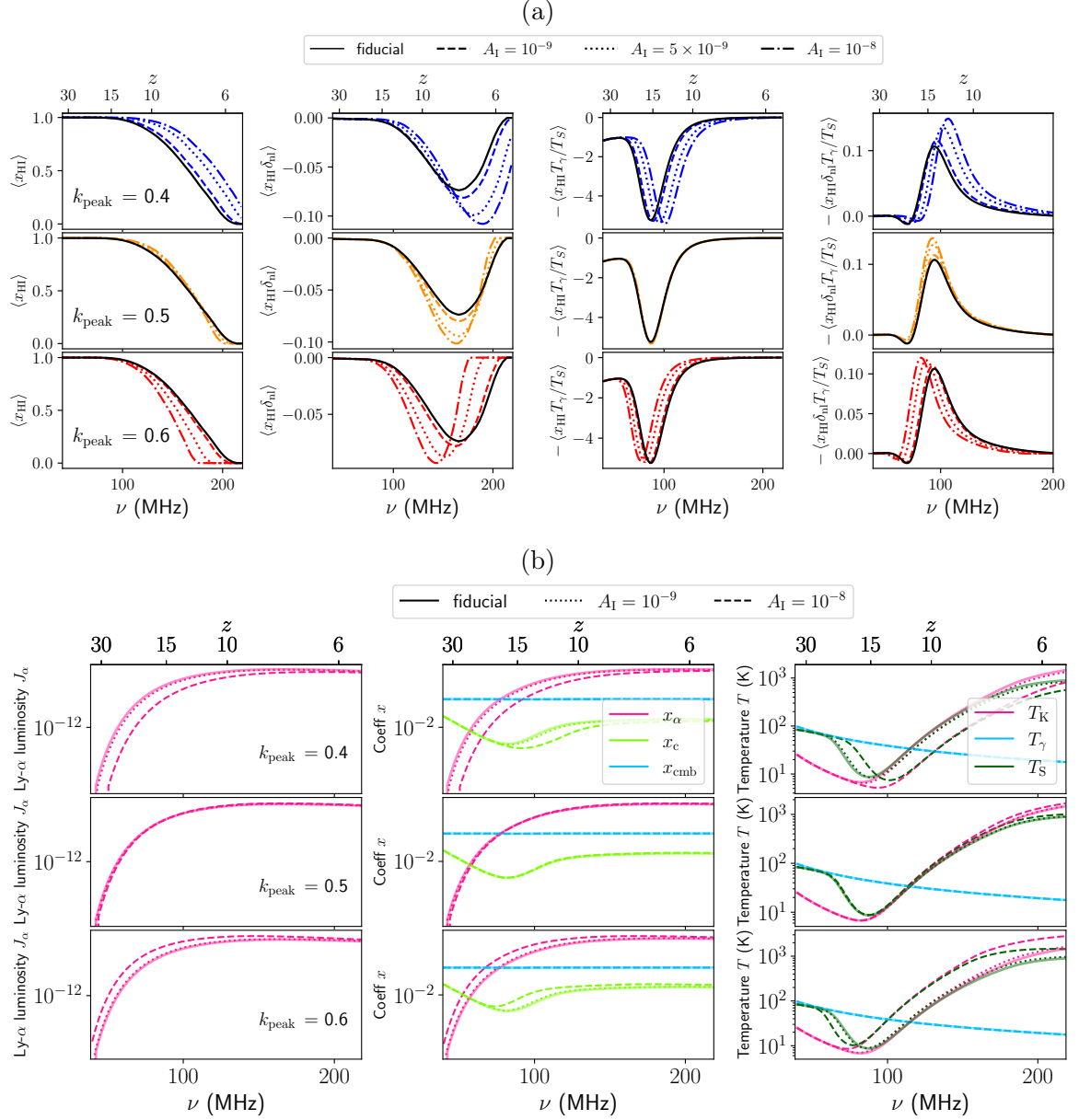


Figure 13: (a) The average quantities appearing on the right-hand side of eq. (A.2) for the fiducial and bump models. The top, middle, and bottom panels correspond to k_{peak} values of 0.4, 0.5, and 0.6, respectively. The value of A_{I} are shown by different line styles. (b) The three columns show the total Ly- α luminosity, coupling coefficients, and evolution of the average temperatures for the fiducial and bump models.

take the average of the above equation and obtain the following:

$$\left\langle \delta T_b \right\rangle = C(z) \left[\left\langle x_{\text{HI}} \right\rangle + \left\langle x_{\text{HI}} \delta_{\text{nl}} \right\rangle - \left\langle x_{\text{HI}} \frac{T_\gamma}{T_S} \right\rangle - \left\langle x_{\text{HI}} \delta_{\text{nl}} \frac{T_\gamma}{T_S} \right\rangle \right], \quad (\text{A.2})$$

where

$$C(z) = 27 \left(\frac{\Omega_b h^2}{0.023} \right) \left(\frac{0.15}{\Omega_M h^2} \right)^{1/2} \left(\frac{1}{10} \right)^{1/2} (1+z)^{1/2}. \quad (\text{A.3})$$

The averaged quantities on the right hand side of the above equation are plotted for three values of k_{peak} in the three rows of figure 13(a). As previously noticed, the effects on all the quantities are quite opposite for $k_{\text{peak}} < k^{\text{turn}}$ and $k_{\text{peak}} > k^{\text{turn}}$. The effects of the amplitude parameter are shown by different linestyles. Focusing on the middle panel, where $k_{\text{peak}} \sim k^{\text{turn}}$, the contributions of the bump-like features are prominent in the quantities $\langle x_{\text{HI}} \delta_{\text{nl}} \rangle$ and $-\langle x_{\text{HI}} \delta_{\text{nl}} \frac{T_\gamma}{T_S} \rangle$ due to the density fluctuations, δ_{nl} . However, the other two quantities, $\langle x_{\text{HI}} \rangle$ and $-\langle x_{\text{HI}} \frac{T_\gamma}{T_S} \rangle$, which are independent of δ_{nl} , are relatively insensitive to variation of A_I for $k_{\text{peak}} \sim 0.5$. In addition, the spin temperature T_S is calculated as follows:

$$T_S^{-1} = \frac{x_{\text{cmb}} T_\gamma^{-1} + x_\alpha T_K^{-1} + x_c T_K^{-1}}{x_{\text{cmb}} + x_\alpha + x_c}, \quad (\text{A.4})$$

where x_{cmb} , x_α and x_c are the coupling coefficients due to interactions with the CMB photons, Ly- α photons and collisions, respectively. T_K and T_γ are the kinetic temperature and CMB temperature, respectively. We plot all these quantities for the three cases of bump models in figure 13(b). The redshift evolution of the Ly- α luminosity is also plotted in the first column. Consistent with the previous arguments, the distinct behaviour of bump-like features for k_{peak} above and below k^{turn} and negligible effects for $k_{\text{peak}} \sim k^{\text{turn}}$ is apparent in all of the plots. The major quantity that influences these parameters is the collapsed fraction, f_{coll} , which depends on the halo mass function, as discussed in section 4.2. If $k_{\text{peak}} < k^{\text{turn}}$ ($> k^{\text{turn}}$), the structure formation is driven by a low (high) number of low-mass galaxies compared to the fiducial model, which is also evident from the suppressed (enhanced) Ly- α luminosity at every redshift.

B Relation between the peak of the primordial features and mass of the halos

As discussed in section 4.2, the peak of the primordial features, k_{peak} , can be linked to a halo mass scale M_{peak}^R by comparing the spatial scale ($2\pi/k_{\text{peak}}$) to the radius of the top-hat window function. This relationship between k_{peak} and M_{peak} is shown in Figure 14.

In addition, the variance of density fluctuations, $\sigma^2(M, z=0)$, and the HMF for the bump models shown in Figure 4 indicate that as k_{peak} increases, the mass scales associated with the peak of the profile, i.e., $M_{\text{peak}}^{\sigma^2}$ and $M_{\text{peak}}^{\text{HMF}}$, shifts to lower values. The corresponding k_{peak} and M_{peak} values are also plotted in Figure 14 for comparison.

We note that the $M_{\text{peak}}^{\sigma^2}$ and $M_{\text{peak}}^{\text{HMF}}$ exhibit a similar anti-correlation with k_{peak} , as expected, with a shift in amplitude.

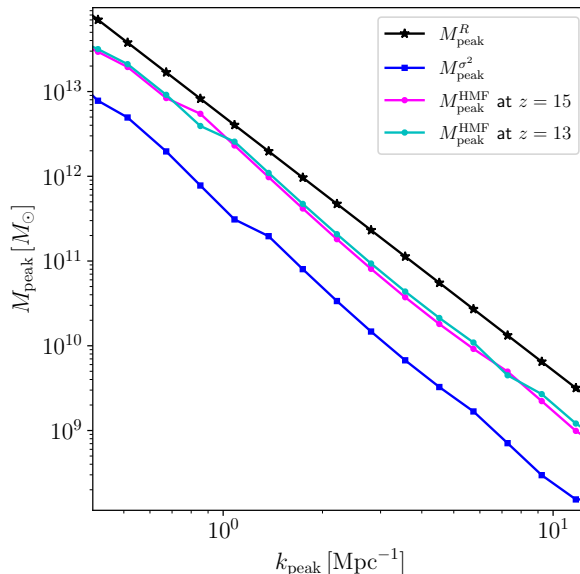


Figure 14: The relation between k_{peak} and M_{peak}^R calculated using the window function is plotted in black. The values of $M_{\text{peak}}^{\sigma^2}$, i.e., mass scale associated with k_{peak} derived from $\sigma^2(M, z = 0)$ in figure 4, are shown in blue. The magenta and cyan lines represent $M_{\text{peak}}^{\text{HMF}}$ at redshifts $z = 15$ and $z = 13$, respectively.

C Collapsed fraction of the halos

In this section, we show the effects of bump-like primordial features on the collapsed fraction of halos, f_{coll} . The ionization fraction and the spin temperature depend on f_{coll} and, therefore, affect the differential brightness temperature of the 21 cm line.

The HMF calculated from the Sheth - Tormen mass function is used to estimate the collapsed fraction of the halos, f_{coll} , given by the fraction of mass contained in halos with mass greater than a threshold M_{min} at redshift z . The redshift dependence of the collapsed fractions for the primordial features is plotted in figure 15. Following our earlier argument, it can be noticed from the figure that, at a given redshift z , a bump-like feature that peaks at $k_{\text{peak}} < k^{\text{turn}} (> k^{\text{turn}})$ [Mpc $^{-1}$] shows a lower (higher) collapsed fraction as it slows down (speeds up) the structure formation, which further results in delayed (earlier) end of reionization. For the case of a bump at 0.5 Mpc $^{-1}$, the deviation from the fiducial model is not significant enough to alter the reionization history and the global 21 cm profile.

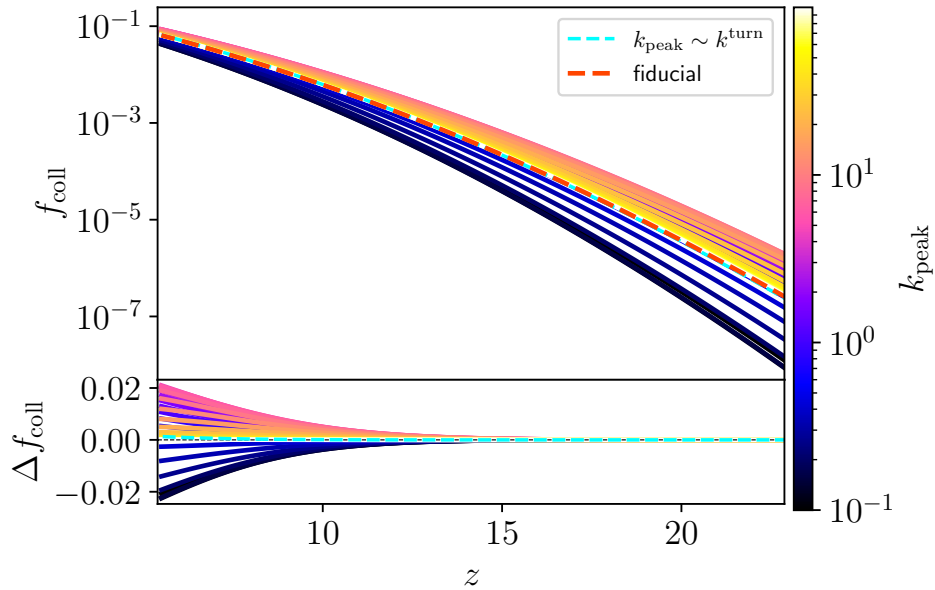


Figure 15: [Top] The collapsed fraction f_{coll} for the fiducial model and bump models. [Bottom] Difference in the collapsed fraction of the bump models relative to the fiducial model, i.e., $\Delta f_{\text{coll}} = f_{\text{coll}}^{\text{bump}} - f_{\text{coll}}^{\text{fid}}$.

References

- [1] A.H. Guth, *Inflationary universe: A possible solution to the horizon and flatness problems*, *Phys. Rev. D* **23** (1981) 347.
- [2] A. Linde, *A new inflationary universe scenario: A possible solution of the horizon, flatness, homogeneity, isotropy and primordial monopole problems*, *Physics Letters B* **108** (1982) 389.
- [3] A. Albrecht and P.J. Steinhardt, *Cosmology for grand unified theories with radiatively induced symmetry breaking*, *Phys. Rev. Lett.* **48** (1982) 1220.
- [4] A. Starobinsky, *A new type of isotropic cosmological models without singularity*, *Physics Letters B* **91** (1980) 99.
- [5] K. Sato, *First-order phase transition of a vacuum and the expansion of the Universe*, *Monthly Notices of the Royal Astronomical Society* **195** (1981) 467 [<https://academic.oup.com/mnras/article-pdf/195/3/467/4065201/mnras195-0467.pdf>].
- [6] D. Kazanas, *Dynamics of the universe and spontaneous symmetry breaking*, *ApJ* **241** (1980) L59.
- [7] PLANCK collaboration, *Planck 2018 results. X. Constraints on inflation*, *Astron. Astrophys.* **641** (2020) A10 [[1807.06211](https://arxiv.org/abs/1807.06211)].
- [8] J. Chluba, J. Hamann and S.P. Patil, *Features and New Physical Scales in Primordial Observables: Theory and Observation*, *Int. J. Mod. Phys. D* **24** (2015) 1530023 [[1505.01834](https://arxiv.org/abs/1505.01834)].
- [9] F. Beutler, M. Biagetti, D. Green, A. Slosar and B. Wallisch, *Primordial Features from Linear to Nonlinear Scales*, *Phys. Rev. Res.* **1** (2019) 033209 [[1906.08758](https://arxiv.org/abs/1906.08758)].
- [10] V. Iršič, M. Viel, M.G. Haehnelt, J.S. Bolton and G.D. Becker, *First constraints on fuzzy dark matter from Lyman- α forest data and hydrodynamical simulations*, *Phys. Rev. Lett.* **119** (2017) 031302 [[1703.04683](https://arxiv.org/abs/1703.04683)].

- [11] B. Abolfathi, D.S. Aguado, G. Aguilar, C. Allende Prieto, A. Almeida, T.T. Ananna et al., *The Fourteenth Data Release of the Sloan Digital Sky Survey: First Spectroscopic Data from the Extended Baryon Oscillation Spectroscopic Survey and from the Second Phase of the Apache Point Observatory Galactic Evolution Experiment*, *ApJS* **235** (2018) 42 [1707.09322].
- [12] DES collaboration, *Dark Energy Survey Year 1 results: Cosmological constraints from cosmic shear*, *Phys. Rev. D* **98** (2018) 043528 [1708.01538].
- [13] D.J.H. Chung, E.W. Kolb, A. Riotto and I.I. Tkachev, *Probing Planckian physics: Resonant production of particles during inflation and features in the primordial power spectrum*, *Phys. Rev. D* **62** (2000) 043508 [hep-ph/9910437].
- [14] N. Barnaby, Z. Huang, L. Kofman and D. Pogosyan, *Cosmological Fluctuations from Infra-Red Cascading During Inflation*, *Phys. Rev. D* **80** (2009) 043501 [0902.0615].
- [15] N. Barnaby and Z. Huang, *Particle Production During Inflation: Observational Constraints and Signatures*, *Phys. Rev. D* **80** (2009) 126018 [0909.0751].
- [16] L. Pearce, M. Peloso and L. Sorbo, *Resonant particle production during inflation: a full analytical study*, *JCAP* **1705** (2017) 054 [1702.07661].
- [17] K. Furuuchi, *Excursions through KK modes*, *JCAP* **1607** (2016) 008 [1512.04684].
- [18] K. Furuuchi, S.S. Naik and N.J. Jobu, *Large Field Excursions from Dimensional (De)construction*, *JCAP* **06** (2020) 054 [2001.06518].
- [19] K. Furuuchi, N.J. Jobu and S.S. Naik, *Extra-Natural Inflation (De)constructed*, [2004.13755](https://arxiv.org/abs/2004.13755).
- [20] S.S. Naik, K. Furuuchi and P. Chingangbam, *Particle production during inflation: a Bayesian analysis with CMB data from Planck 2018*, *JCAP* **07** (2022) 016 [2202.05862].
- [21] M. Ballardini, F. Finelli, F. Marulli, L. Moscardini and A. Veropalumbo, *New constraints on primordial features from the galaxy two-point correlation function*, [2202.08819](https://arxiv.org/abs/2202.08819).
- [22] <http://www.skatelescope.org/>.
- [23] D.R. DeBoer et al., *Hydrogen Epoch of Reionization Array (HERA)*, *Publ. Astron. Soc. Pac.* **129** (2017) 045001 [1606.07473].
- [24] D.C. Price, L.J. Greenhill, A. Fialkov, G. Bernardi, H. Garsden, B.R. Barsdell et al., *Design and characterization of the Large-aperture Experiment to Detect the Dark Age (LEDA) radiometer systems*, *MNRAS* **478** (2018) 4193 [1709.09313].
- [25] H.W. Edler, F. de Gasperin and D. Rafferty, *Investigating ionospheric calibration for LOFAR 2.0 with simulated observations*, *A&A* **652** (2021) A37 [2105.04636].
- [26] R.B. Wayth, S.J. Tingay, C.M. Trott, D. Emrich, M. Johnston-Hollitt, B. McKinley et al., *The Phase II Murchison Widefield Array: Design overview*, *PASA* **35** (2018) e033 [1809.06466].
- [27] F. Acero, J.T. Acquaviva, R. Adam, N. Aghanim, M. Allen, M. Alves et al., *French SKA White Book - The French Community towards the Square Kilometre Array*, *arXiv e-prints* (2017) [arXiv:1712.06950](https://arxiv.org/abs/1712.06950) [1712.06950].
- [28] J.D. Bowman, A.E.E. Rogers and J.N. Hewitt, *Toward Empirical Constraints on the Global Redshifted 21 cm Brightness Temperature During the Epoch of Reionization*, *Astrophys. J.* **676** (2008) 1 [0710.2541].
- [29] N. Patra, R. Subrahmanyan, A. Raghunathan and N. Udaya Shankar, *SARAS: a precision system for measurement of the cosmic radio background and signatures from the epoch of reionization*, *Experimental Astronomy* **36** (2013) 319 [1211.3800].
- [30] S. Singh, R. Subrahmanyan, N.U. Shankar, M.S. Rao, B.S. Girish, A. Raghunathan et al., *SARAS 2: A Spectral Radiometer for probing Cosmic Dawn and the Epoch of Reionization through detection of the global 21 cm signal*, *Exper. Astron.* **45** (2018) 269 [1710.01101].

- [31] M. Sokolowski, S.E. Tremblay, R.B. Wayth, S.J. Tingay, N. Clarke, P. Roberts et al., *BIGHORNS - Broadband Instrument for Global Hydrogen Reionisation Signal*, *PASA* **32** (2015) e004 [[1501.02922](#)].
- [32] L. Philip, Z. Abdurashidova, H.C. Chiang, N. Ghazi, A. Gumba, H.M. Heilgendorff et al., *Probing Radio Intensity at High-Z from Marion: 2017 Instrument*, *Journal of Astronomical Instrumentation* **8** (2019) 1950004 [[1806.09531](#)].
- [33] E. de Lera Acedo, D.I.L. de Villiers, N. Razavi-Ghods, W. Handley, A. Fialkov, A. Magro et al., *Author Correction: The REACH radiometer for detecting the 21-cm hydrogen signal from redshift $z \approx 7.5$ -28*, *Nature Astronomy* **6** (2022) 1332.
- [34] R.A. Monsalve, C. Altamirano, V. Bidula, R. Bustos, C.H. Bye, H.C. Chiang et al., *Mapper of the IGM spin temperature: instrument overview*, *MNRAS* **530** (2024) 4125 [[2309.02996](#)].
- [35] P. Bull, A. El-Makadema, H. Garsden, J. Edgley, N. Roddis, J. Chluba et al., *RHINO: A large horn antenna for detecting the 21cm global signal*, *arXiv e-prints* (2024) [arXiv:2410.00076](#) [[2410.00076](#)].
- [36] M. Klein Wolt, H. Falcke and L. Koopmans, *The Astronomical Lunar Observatory (ALO) - Probing the cosmological Dark Ages and Cosmic Dawn with a distributed low-frequency radio array on the Lunar Far Side*, in *American Astronomical Society Meeting Abstracts*, vol. 243 of *American Astronomical Society Meeting Abstracts*, p. 264.01, Feb., 2024.
- [37] J.O. Burns, R. MacDowall, S. Bale, G. Hallinan, N. Bassett and A. Hegedus, *Low Radio Frequency Observations from the Moon Enabled by NASA Landed Payload Missions*, *PSJ* **2** (2021) 44 [[2102.02331](#)].
- [38] S.D. Bale, N. Bassett, J.O. Burns, J. Dorigo Jones, K. Goetz, C. Hellum-Bye et al., *LuSEE 'Night': The Lunar Surface Electromagnetics Experiment*, *arXiv e-prints* (2023) [arXiv:2301.10345](#) [[2301.10345](#)].
- [39] M. Sathyanarayana Rao, S. Singh, S. K. S., G. B. S., K. Sathish, R. Somashekar et al., *PRATUSH experiment concept and design overview*, *Experimental Astronomy* **56** (2023) 741.
- [40] J.R. Pritchard and A. Loeb, *21-cm cosmology*, *Rept. Prog. Phys.* **75** (2012) 086901 [[1109.6012](#)].
- [41] S.S. Naik, P. Chingangbam and K. Furuuchi, *Particle production during inflation: constraints expected from redshifted 21 cm observations from the epoch of reionization*, *JCAP* **04** (2023) 058 [[2212.14064](#)].
- [42] S. Yoshiura, K. Takahashi and T. Takahashi, *Probing Small Scale Primordial Power Spectrum with 21cm Line Global Signal*, *Phys. Rev. D* **101** (2020) 083520 [[1911.07442](#)].
- [43] J.B. Muñoz, C. Dvorkin and F.-Y. Cyr-Racine, *Probing the Small-Scale Matter Power Spectrum with Large-Scale 21-cm Data*, *Phys. Rev. D* **101** (2020) 063526 [[1911.11144](#)].
- [44] S. Furlanetto, S.P. Oh and F. Briggs, *Cosmology at Low Frequencies: The 21 cm Transition and the High-Redshift Universe*, *Phys. Rept.* **433** (2006) 181 [[astro-ph/0608032](#)].
- [45] S.R. Furlanetto, A. Lidz, A. Loeb, M. McQuinn, J.R. Pritchard, P.R. Shapiro et al., *Cosmology from the Highly-Redshifted 21 cm Line*, in *astro2010: The Astronomy and Astrophysics Decadal Survey*, vol. 2010, p. 82, Jan., 2009 [[0902.3259](#)].
- [46] J.R. Pritchard and A. Loeb, *21 cm cosmology in the 21st century*, *Reports on Progress in Physics* **75** (2012) 086901 [[1109.6012](#)].
- [47] A. Mesinger, *The Cosmic 21-cm Revolution; Charting the first billion years of our universe* (2019), [10.1088/2514-3433/ab4a73](#).
- [48] P. Madau, A. Meiksin and M.J. Rees, *21-CM tomography of the intergalactic medium at high redshift*, *Astrophys. J.* **475** (1997) 429 [[astro-ph/9608010](#)].

- [49] R. Barkana and A. Loeb, *In the beginning: The First sources of light and the reionization of the Universe*, *Phys. Rept.* **349** (2001) 125 [[astro-ph/0010468](#)].
- [50] A. Mesinger, S. Furlanetto and R. Cen, *21CMFAST: a fast, seminumerical simulation of the high-redshift 21-cm signal*, *Mon. Not. Roy. Astron. Soc.* **411** (2011) 955 [[1003.3878](#)].
- [51] S.G. Murray, B. Greig, A. Mesinger, J.B. Muñoz, Y. Qin, J. Park et al., *21cmFAST v3: A Python-integrated C code for generating 3D realizations of the cosmic 21cm signal*, *J. Open Source Softw.* **5** (2020) 2582 [[2010.15121](#)].
- [52] J. Park, A. Mesinger, B. Greig and N. Gillet, *Inferring the astrophysics of reionization and cosmic dawn from galaxy luminosity functions and the 21-cm signal*, *Mon. Not. Roy. Astron. Soc.* **484** (2019) 933 [[1809.08995](#)].
- [53] D.J. Eisenstein and W. Hu, *Baryonic features in the matter transfer function*, *Astrophys. J.* **496** (1998) 605 [[astro-ph/9709112](#)].
- [54] D.J. Eisenstein and W. Hu, *Power spectra for cold dark matter and its variants*, *Astrophys. J.* **511** (1997) 5 [[astro-ph/9710252](#)].
- [55] W.H. Press and P. Schechter, *Formation of Galaxies and Clusters of Galaxies by Self-Similar Gravitational Condensation*, *ApJ* **187** (1974) 425.
- [56] R.K. Sheth and G. Tormen, *An Excursion Set Model of Hierarchical Clustering : Ellipsoidal Collapse and the Moving Barrier*, *Mon. Not. Roy. Astron. Soc.* **329** (2002) 61 [[astro-ph/0105113](#)].
- [57] A. Jenkins, C.S. Frenk, S.D.M. White, J.M. Colberg, S. Cole, A.E. Evrard et al., *The mass function of dark matter haloes*, *MNRAS* **321** (2001) 372 [[astro-ph/0005260](#)].
- [58] B. Greig and A. Mesinger, *Simultaneously constraining the astrophysics of reionization and the epoch of heating with 21CMMC*, *Mon. Not. Roy. Astron. Soc.* **472** (2017) 2651 [[1705.03471](#)].
- [59] A. Cohen, A. Fialkov, R. Barkana and M. Lotem, *Charting the Parameter Space of the Global 21-cm Signal*, *Mon. Not. Roy. Astron. Soc.* **472** (2017) 1915 [[1609.02312](#)].
- [60] PLANCK collaboration, *Planck 2015 results. XX. Constraints on inflation*, *Astron. Astrophys.* **594** (2016) A20 [[1502.02114](#)].
- [61] PLANCK collaboration, *Planck 2018 results. VI. Cosmological parameters*, *Astron. Astrophys.* **641** (2020) A6 [[1807.06209](#)].
- [62] I. McGreer, A. Mesinger and V. D’Odorico, *Model-independent evidence in favour of an end to reionization by $z \approx 6$* , *Mon. Not. Roy. Astron. Soc.* **447** (2015) 499 [[1411.5375](#)].
- [63] X. Jin et al., *(Nearly) Model-independent Constraints on the Neutral Hydrogen Fraction in the Intergalactic Medium at $z \sim 5-7$ Using Dark Pixel Fractions in Ly α and Ly β Forests*, *Astrophys. J.* **942** (2023) 59 [[2211.12613](#)].
- [64] Y. Zhu et al., *Long Dark Gaps in the Ly β Forest at $z < 6$: Evidence of Ultra-late Reionization from XQR-30 Spectra*, *Astrophys. J.* **932** (2022) 76 [[2205.04569](#)].
- [65] B. Greig et al., *IGM damping wing constraints on the tail end of reionization from the enlarged XQR-30 sample*, *Mon. Not. Roy. Astron. Soc.* **530** (2024) 3208 [[2404.12585](#)].
- [66] Y. Zhu et al., *Damping wing-like features in the stacked Ly α forest: Potential neutral hydrogen islands at $z < 6$* , *Mon. Not. Roy. Astron. Soc.* **533** (2024) L49 [[2405.12275](#)].
- [67] B. Spina, S.E.I. Bosman, F.B. Davies, P. Gaikwad and Y. Zhu, *Damping wings in the Lyman- α forest: a model-independent measurement of the neutral fraction at $5.4 < z < 6.1$* , *Astron. Astrophys.* **688** (2024) L26 [[2405.12273](#)].
- [68] C.A. Mason, T. Treu, M. Dijkstra, A. Mesinger, M. Trenti, L. Pentericci et al., *The Universe Is Reionizing at $z \sim 7$: Bayesian Inference of the IGM Neutral Fraction Using Ly α Emission from Galaxies*, *Astrophys. J.* **856** (2018) 2 [[1709.05356](#)].

- [69] C.A. Mason et al., *Inferences on the timeline of reionization at $z \sim 8$ from the KMOS Lens-Amplified Spectroscopic Survey*, *Mon. Not. Roy. Astron. Soc.* **485** (2019) 3947 [[1901.11045](#)].
- [70] A. Hoag, M. Bradač, K. Huang, C. Mason, T. Treu, K.B. Schmidt et al., *Constraining the Neutral Fraction of Hydrogen in the IGM at Redshift 7.5*, *ApJ* **878** (2019) 12 [[1901.09001](#)].
- [71] L.R. Whittler, C.A. Mason, K. Ren, M. Dijkstra, A. Mesinger, L. Pentericci et al., *The Impact of Scatter in the Galaxy UV Luminosity to Halo Mass Relation on Ly α Visibility During the Epoch of Reionization*, [1911.03499](#).
- [72] I. Jung, S.L. Finkelstein, M. Dickinson, T.A. Hutchison, R.L. Larson, C. Papovich et al., *Texas Spectroscopic Search for Ly α Emission at the End of Reionization. III. The Ly α Equivalent-width Distribution and Ionized Structures at $z > 7$* , *ApJ* **904** (2020) 144 [[2009.10092](#)].
- [73] A.M. Morales, C.A. Mason, S. Bruton, M. Gronke, F. Haardt and C. Scarlata, *The Evolution of the Lyman-alpha Luminosity Function during Reionization*, *Astrophys. J.* **919** (2021) 120 [[2101.01205](#)].
- [74] P. Bolan, B.C. Lemaux, C. Mason, M. Bradač, T. Treu, V. Strait et al., *Inferring the intergalactic medium neutral fraction at z 6-8 with low-luminosity Lyman break galaxies*, *MNRAS* **517** (2022) 3263 [[2111.14912](#)].
- [75] I.G.B. Wold, S. Malhotra, J. Rhoads, J. Wang, W. Hu, L.A. Perez et al., *LAGER Ly α Luminosity Function at z 7: Implications for Reionization*, *ApJ* **927** (2022) 36 [[2105.12191](#)].
- [76] T. Morishita, G. Roberts-Borsani, T. Treu, G. Brammer, C.A. Mason, M. Trenti et al., *Early Results from GLASS-JWST. XIV. A Spectroscopically Confirmed Protocluster 650 Million Years after the Big Bang*, *ApJ* **947** (2023) L24 [[2211.09097](#)].
- [77] S. Bruton, Y.-H. Lin, C. Scarlata and M.J. Hayes, *The Universe is at Most 88% Neutral at $z = 10.6$* , *ApJ* **949** (2023) L40 [[2303.03419](#)].
- [78] T.Y.-Y. Hsiao et al., *JWST NIRSpec Spectroscopy of the Triply Lensed $z = 10.17$ Galaxy MACS0647-JD*, *Astrophys. J.* **973** (2024) 8 [[2305.03042](#)].
- [79] M. Tang, D.P. Stark, M.W. Topping, C. Mason and R.S. Ellis, *JWST/NIRSpec Observations of Ly α Emission in Star Forming Galaxies at $6.5 \lesssim z \lesssim 13$* , [2408.01507](#).
- [80] E. Curtis-Lake, S. Carniani, A. Cameron, S. Charlot, P. Jakobsen, R. Maiolino et al., *Spectroscopic confirmation of four metal-poor galaxies at $z = 10.3$ - 13.2* , *Nature Astronomy* **7** (2023) 622 [[2212.04568](#)].
- [81] M. Nakane, M. Ouchi, K. Nakajima, Y. Harikane, Y. Ono, H. Umeda et al., *Ly α Emission at $z = 7$ - 13 : Clear Evolution of Ly α Equivalent Width Indicating a Late Cosmic Reionization History*, *ApJ* **967** (2024) 28 [[2312.06804](#)].